SELF-PHASE MODULATION INDUCED SPECTRAL BROADENING IN A STRETCHED HOLLOW-CORE FIBER FOR SUB-30 FEMTOSECOND PULSE COMPRESSION

by

RYAN THOMPSON BARCO

(Under the Direction of Susanne Ullrich)

ABSTRACT

This thesis develops a stretched hollow-core fiber system capable of spectrally broadening 130fs pulses generated from a commercial Ti:Sa Coherent laser system for subsequent prism-based post-compression, achieving sub-30fs pulses. The effects of various fiber core diameters on spectral broadening were examined. Nitrogen and argon gases were independently tested as nonlinear media within the hollow-core fiber, with argon demonstrating superior broadening characteristics and being selected as the optimal medium. Spectral broadening of ultraviolet pulses at 400nm and 267nm wavelengths, resulted in bandwidths corresponding to sub-20 fs pulses in the transform-limited case. At 267nm, the influence of input pulse energy, argon pressure, and the long-term stability of the hollow-core fiber setup were systematically studied. A double-pass ultraviolet fused silica prism pair compressor was experimentally optimized to generate sub-30fs pulses, which were characterized using transient grating frequency-resolved optical gating (TG-FROG).

INDEX WORDS: Ultrafast Spectroscopy, Non-linear optics, Self-Phase Modulation, Femtosecond Pulse Compression

SELF-PHASE MODULATION INDUCED SPECTRAL BROADENING IN A STRETCHED HOLLOW-CORE FIBER FOR SUB-30 FS PULSE COMPRESSION

by

RYAN THOMPSON BARCO

B.S., The University of South Florida, 2017

A Thesis Submitted to the Graduate Faculty of The University of Georgia in Partial Fulfillment of the Requirements for the Degree

MASTER OF SCIENCE

ATHENS, GEORGIA

2025

SELF-PHASE MODULATION INDUCED SPECTRAL BROADENING IN A STRETCHED HOLLOW-CORE FIBER FOR SUB-30 FS PULSE COMPRESSION

by

RYAN THOMPSON BARCO

Major Professor:	Susanne Ullrich
Committee:	Peter Kner
	Tho Nguyen

Electronic Version Approved:

Ron Walcott
Vice Provost for Graduate Education and Dean of the Graduate School
The University of Georgia
May 2025

ACKNOWLEDGEMENTS

Starting this section has proven to be the hardest part of the write-up in this thesis. Ensuring I include all those who lent a helping hand will prove to be a losing battle. To those I may mistakenly omit, know that your contributions were greatly appreciated.

As is only right, I want to begin by thanking my advising professor Dr. Susanne Ullrich for all her insight and help working on this rewarding project. Beginning this project, I believed my background in R&D fiber optics would simplify this task but as I came to find in the world of ultrafast nonlinear optics, nothing is ever as simple. Your expertise in the field and willingness to always offer guidance proved invaluable to me over the duration of this work.

To my lab mates Yingqi Qu, Moti Chudali, Bijay Duwal, and Mehade Hasan I cannot thank you all enough for the assistance you have provided me with in the lab. Whether it being as simple as turning on the laser in the morning, or the painstaking work of optimizing the transient grating FROG setup, it was all greatly appreciated.

Furthermore, to those in my cohort, Thilanka Liyanage, Thomas Carroll, Evan Garbe, and Zain Charania you all made my time at the University of Georgia truly unforgettable. Whether it be completing a Dr. G homework set or a Thursday night at Cutter's Pub, every moment was enjoyed to the fullest.

To my father and mother, Thomas and Lisa Barco, words cannot do justice to the love, assistance, and encouragement the two of you have always extended me. I am in the position I am today because of you. In an effort to keep the acknowledgements shorter than the work of my

thesis I'll simply say thank you both so much and I love you two more than I can properly express in words.

Lastly but most importantly, to my best friend and the love of my life Anh Thu Nguyen, you are the reason I am finalizing my thesis with this segment. You were with me through the highs and lows, encouraging me at every step of the way. I look forward to the next chapter of our life together and with the deepest gratitude, I am truly grateful for you.

TABLE OF CONTENTS

Page

LIST OF TABLES

Page

LIST OF FIGURES

Page

CHAPTER 1

INTRODUCTION

Ultrafast spectroscopy generally defines the study of how light interacts with matter on an extremely small timescale. To a large extent, it is the study of excitation dynamics of electron energy states but also encompasses the observations of various nonlinear optical effects, such as stimulated Raman scatter, among other phenomenon as well. The ultrafast timescale has been defined as having a time resolution on the order of picoseconds (10^{-12} s) to femtoseconds (10^{-15} s) [1]. With time resolution on the scale of quadrillionths of a second, this variant of spectroscopy has proven to be invaluable to a wide array of studies. Research fields such as semiconductors [2], medicinal sciences [3], atmospheric science [4], intense laser physics, and most famously in the realm of femtochemistry where Ahmed Hassan Zewail was awarded the Nobel Prize in chemistry for his work studying the formation and breaking of molecular bonds in real time at the turn of the 21st century [5].

Currently, the world of laser systems that can supply high peak power and ultrashort pulses is well-established and thriving, with many commercially available systems operating off titanium-sapphire (Ti:Sa) Kerr lens mode locking lasers. Some of which can provide few-cycle pulse durations down to ~5fs. However, these systems are designed for specific case scenarios where pulse duration and peak pulse energy (among other parameters) must be compromised. For example, a Ti:Sa 5fs pulse duration will have lower output pulse energy (μJ scale) than that of Ti:Sa system outputting >100fs pulses (mJ-J). Not only can fiber-based pulse compression systems maintain higher energies while generating ultrashort pulses compared to shorter pulse

duration lasers, but they also allow for spectral supercontinuum generation. This capability allows for a wide range of wavelengths to be accessible, making fiber setups a highly versatile tool for spectroscopy. Many research labs have replaced their optical parametric amplifiers (OPA) with hollow-core and photonic fibers for this very reason [6]. In general, fiber-based supercontinuum sources offer less pulse energy loss, broader wavelength selection, increased stability, and are far cheaper to create and maintain than that of OPAs!

This thesis serves the purpose for the creation of a low-cost, easily adjustable, and stable stretched hollow-core fiber (HCF) setup that will take nominally 130fs pulse duration input pulses and compress them down to the sub-30fs regime. Another aspect of interest regarding this setup is the low energy regime at which compressed UV pulses are generated, where only a few tens of microjoule input energy is supplied. The HCF system will reach sub-30fs pulses through the nonlinear process known as self-phase modulation (SPM). Pulse compression relies on the relationship between a wave's temporal and spectral bandwidth, which are most frequently defined as the full width at half maximum (FWHM) of the respective bandwidths. Simply put, if one were to spectrally broaden a pulse through SPM, then the pulse duration of that pulse can approach shorter durations with increased broadening. Thus, there is a trade-off between decreased spectral detail and improved time resolution.

The theoretical background relevant to this thesis for the creation of sub-30fs pulses will be explained in greater detail in the following chapter. After which, the experimental setup and procedure for operation of the stretched hollow-core fiber system will be provided, followed by the experimental results obtained. To conclude, a summary and outlook of the HCF system will be presented.

CHAPTER 2

THEORETICAL BACKGROUND

The purpose of this background is to lay the foundation for all aspects of interest when coupling ultrafast pulses into a hollow-core fiber (HCF) for post-compression as relevant to this thesis. Gaussian beam electric field and intensity representation, nonlinear optical effects of interest, group velocity dispersion (GVD), the time-bandwidth product (TBP), and HCF transmission efficiency conditions will all be covered within this chapter.

To begin with, the choice of using a stretched hollow-core fiber rather than a few other frequently used alternatives for spectral broadening should be explained. Self-phase modulation (SPM) requires intense pulses of energy over an extended length to broaden an input pulse to a desired bandwidth. If one were to use a long focal lens (on the order of a few meters) inside of a gas cell, this would provide a depth of field (DOF) in the range of several centimeters, limiting the range over which SPM may occur. Additionally, longer focal lengths equate to larger focused spot sizes, which consequently produce less intense focal spots. One may suggest increasing the diameter of the beam at the focal lens to generate smaller focal spot sizes, however, the tradeoff is a shorter DOF. Practically speaking, a long multimeter focal lens is not always a feasible option within a lab setup.

Another option that may be proposed is the use of a solid waveguide. Solid waveguides have higher indices of refraction and better mode confinement when a pulse is coupled into the fiber. A higher refractive index induces stronger nonlinear effects, and the improved mode confinement allows for more energy to stay within the core of the fiber compared against HCF.

However, a solid core does not allow for dispersion tuning, as a pressure-controlled gas cell can no longer be used. Additionally, solid waveguides are more prone than hollow-core fibers to interface damage from exceedingly energetic pulses, which is exceptionally problematic in the ultrafast laser regime, as peak pulse energy tends to be very high.

HCF addresses the issues associated with a gas cell and a solid waveguide. Hollow fibers allow for an extended length of intense light propagation without the need of a multimeter focal lens. Furthermore, a HCF can allow for much more intense light propagation over solid core waveguides, while simultaneously allowing for a pressure tunable environment for desired spectral broadening.

2.1 Gaussian Beam Representation

The formal electric field representation of a gaussian beam that is horizontally polarized along the x-direction and propagating in the z-direction under the paraxial approximation is denoted below in its complex form [7],

$$\vec{E}(x,y,z,t) = \widetilde{E_0}\exp\left(i(kz-\omega_0 t)\right)\hat{x}, \tag{2.1.1}$$

We may also represent real from of the electric field as

$$\vec{E}(x,y,z,t) = Re\left[\vec{E}(x,y,z,t)\right] = \widetilde{E_0}\cos\left(kz-\omega_0 t\right), \tag{2.1.2}$$

where $\widetilde{E_0}$ denotes the transverse amplitude distribution as,

$$\widetilde{E_0}(x,y) = E_0\exp\left(\frac{x^2+y^2}{w(z)^2}\right), \tag{2.1.3}$$

w(z) represents the beam the beam waist radius at position z and has the following form,

$$\mathrm{w(z)} = w_0\left[\left(1+\left(\frac{z}{z_R}\right)^2\right], \tag{2.1.4}$$

Here z_R defines the Rayleigh range which is defined as the position where the initial beam waist cross sectional area doubles in size. The original beam waist is represented as w_0 and is the beam

spot size $\frac{1}{e^2}$ which is measured as the distance required for the intensity of the beam to fall to ~13.5% of the peak intensity.

$$z_R = \frac{\pi {w_0}^2}{\lambda}, \tag{2.1.5}$$

The intensity for such a beam is directly proportional to the square of the electric field,

$$I(x, y, z) = \frac{1}{2}\epsilon_0 c \widetilde{E_0}^2. \tag{2.1.6}$$

2.2 Kerr Effect

Following the introduction of our laser-supplied electric field intensity formalism, the next logical step is to focus on the Kerr effect. In 1875 John Kerr observed that when organic liquids were subject to a supplied electric field from an applied voltage, their intrinsic index of refraction changed [8]. With the advent of the laser in the 1960s, the optically induced electric fields were strong enough to replace the supplied voltage method used by Kerr nearly a century prior. This new method of altering materials index of refraction through laser use became known as the Optical Kerr effect.

To better understand how an intense electric field can induce refractive index change we must consider nonlinear polarization. Polarization is defined as

$$\vec{P} = \epsilon_0 \chi \vec{E} \tag{2.2.1}$$

Where ε_0 is the electric permeability of free space, and $\chi = \varepsilon - 1$ denotes electric susceptibility. If the supplied electric field is strong enough, and the material through which the electric field propagates produces a nonlinear response, the polarization vector can be expanded as

$$\vec{P} = \epsilon_0[\chi^{(1)}\vec{E} + \chi^{(2)}\vec{E}^2 + \chi^{(3)}\vec{E}^3 + \cdots]\,. \tag{2.2.2}$$

In the above expression, the second order term of electric susceptibility may be neglected due to the centrosymmetric geometry of a gas filled cylinder, a HCF in this thesis [9]. Furthermore,

higher ordered terms beyond χ^3 require electric field intensities far greater than what is typically available in a laboratory setting and will be neglected as well. Rearranging equation 2.2.2 gives a clearer view of the linear and nonlinear component of the polarization (eq. 2.2.3) and the effective electric susceptibility (eq. 2.2.7),

$$\vec{P} = \epsilon_0[\chi^{(1)} + \chi^{(3)}\vec{E}^2]\vec{E} \tag{2.2.3}$$

$$\vec{P} = \epsilon_0[\chi^{(1)}\cos(kz - \omega_0 t) + \chi^{(3)}\widetilde{E_0}^2\cos^3(kz - \omega_0 t)]\widetilde{E_0} \tag{2.2.4}$$

$$\vec{P} \approx \epsilon_0[\chi^{(1)}\cos(kz - \omega_0 t) + \frac{3\chi^{(3)}}{4}\widetilde{E_0}^2\cos(kz - \omega_0 t)]\widetilde{E_0} \tag{2.2.5}$$

$$\vec{P} = \epsilon_0[\chi^{(1)} + \tfrac{3\chi^{(3)}}{4}\widetilde{E_0}^2]\widetilde{E_0}\cos(kz - \omega_0 t) \tag{2.2.6}$$

$$\chi_{eff} = \chi^L + \chi^{NL} \tag{2.2.7}$$

the linear and nonlinear term of electric susceptibility are represented as $\chi^L = \chi^{(1)}$ and $\chi^{NL} = \frac{3\chi^{(3)}}{4}\widetilde{E_0}^2$ respectively. Electric permeability may be expressed in in terms of effective electric susceptibility,

$$\varepsilon_r = 1 + \chi_{eff} \tag{2.2.8}$$

$$= [1 + \chi^L + \chi^{NL}] = \varepsilon_L + \varepsilon_{NL} \tag{2.2.9}$$

$$= [1 + \chi^{(1)} + \tfrac{3\chi^{(3)}}{4}\widetilde{E_0}^2]. \tag{2.2.10}$$

The refractive index of a material is defined as

$$n = \sqrt{\varepsilon} \tag{2.2.11}$$

Accounting for linear and nonlinear terms, the index of refraction takes the form

$$n = \sqrt{\varepsilon_0(1 + \chi^{(1)} + \tfrac{3\chi^{(3)}}{4}\widetilde{E_0}^2)} \cong \sqrt{\varepsilon_L + \varepsilon_{NL}}\,. \tag{2.2.12}$$

This square root can be restated under binomial approximation as

$$n \approx \varepsilon_L \left(1 + \frac{\varepsilon_{NL}}{2\varepsilon_L}\right) = n_0 + \frac{3\chi^{(3)}}{8}\widetilde{E_0}^2 \tag{2.2.13}$$

$$n = n_0 + n_2 I(\mathrm{t}) \tag{2.2.13}$$

Finally, we arrive at our nonlinear representation of the Optical Kerr effect induced index of refraction. The linear and nonlinear portion of the intensity dependent index of refraction are represented as $n_0 = 1 + \chi^{(1)}$ and $n_2 = \frac{3\chi^{(3)}}{4c\epsilon_0 {n_0}^2}$.

2.3 Self-Phase Modulation

Self-phase modulation is an intensity dependent phenomenon that causes a spectral phase shift in a propagating wave. Here we will build off the work presented previously in the Optical Kerr effect to see how an intense electric field can lead to an altered spectral phase. Crucial to the work of this thesis, the altered phase will give rise to additional frequencies stemming from our supplied laser pulse's central frequency [10].

Let us begin with the expression of an intense arbitrary wave with a phase denoted as

$$\varphi(t) = \omega_0 t - kz + \varphi_0 \tag{2.3.1}$$

ω_0 represents the central frequency, ϕ_0 the phase constant, and the wavenumber "k" which is dependent on the index of refraction, now carrying an intensity dependence

$$k(I) = \frac{\omega n}{c} = \frac{\omega}{c}(n_0 + n_2 I(t)) \tag{2.3.2}$$

Thus, the time-dependent components of the spectral phase becomes

$$\varphi(t) = \omega_0 t - \frac{\omega z}{c}(n_0 + n_2 I(\mathrm{t})) + \varphi_0 \tag{2.3.3}$$

and the instantaneous frequency of the phase is

$$\omega_{inst}(t) = \frac{d\varphi}{dt} = \omega_0 - \frac{\omega z}{c} n_2 \frac{dI}{dt} \tag{2.3.4}$$

Resulting from this instantaneous frequency shift, the Optical Kerr effect produces an intensity dependence on the index of refraction, altering the spectral phase of the propagating wave. This nonlinear relationship gives rise to additional frequency elements that may blue and red shift as shown in figure 2.3. The leading edge of the pulse associates with lower frequencies while the falling edge corresponds to higher frequencies. This can be seen from equation 2.3.4 where the leading edge has an increasing intensity in time leading to a red shift. Conversly the falling edge has a diminishing intensity which increases $\omega_{inst}(t)$ producing a blue shift.

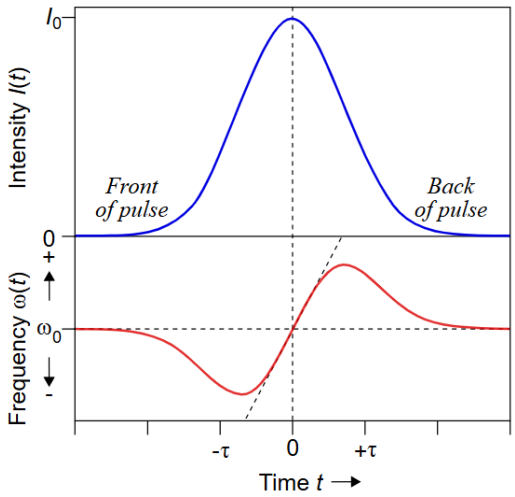

Figure 2.3 Self-phase modulation induced frequency shift. (Source: [11])

The total nonlinear phase shift $\Delta\phi_{NL}$ at the peak of the pulse can be expressed as

$$\Delta\varphi_{NL} = \int_0^L n_2(z)I(z)dz = \frac{2\pi}{\lambda} n_2 I_0 L_{eff} \tag{2.3.5}$$

here λ is defined at the central frequency and I_0 is the maximum intensity of the pulse prior to propagating throughout the nonlinear medium [12]. The effective length "L_{eff}" accounts for changing parameters of the pulse during propagation such as changing nonlinear index of refraction (n_2) and decreasing intensity as the pulse attenuates.

$$L_{eff} = \int_0^L \frac{n_2(z)}{n_n} \cdot \frac{I(z)}{I_0} dz \tag{2.3.6}$$

We have seen the role that pulse intensity and effective length play in inducing a spectral phase shift, one can also selectively choose the nonlinear medium through which the pulse propagates. For the gases which this thesis concerns itself with: atmospheric air, nitrogen, and argon have a nonlinear index of refraction of 5.7, 6.7, and 19.4 respectively at 1 bar of pressure [13]. Furthermore, n_2 is pressure dependent and may be further increased with additional pressure as can be seen in equation 2.3.7 where "P" represents a supplied pressure.

$$n_2(P) = n_2(P_{atm}) \frac{P}{P_{atm}} \tag{2.3.7}$$

2.4 Time-Bandwidth Product

The time-bandwidth product is where we will see the fruits of our labor. The goal of this thesis was the creation of compressed pulses from a fixed pulse duration. We covered the electric field representation of a propagating wave and how that can induce a change refractive index of a medium, as well as how that intensity dependent index of refraction leads to frequency shifts in said wave. Now we can relate this frequency shift to pulse duration.

The TBP is defined as a simple relationship between the temporal and spectral width of a pulse. In the case of a gaussian beam, it takes the form [14]:

$$\Delta\tau \cdot \Delta\nu \approx 0.441 \tag{2.4.1}$$

Although simple in form, this equation carries massive implications for the generation of ultrashort pulses. In the theoretical case, the only limit to how short a pulse can be compressed is defined by its spectral width. The resulting temporal width is known as the transform-limited (TL) pulse duration. In practice, pulse broadening is constrained by a myriad of factors and the TL pulse duration cannot be realized exactly. However, under specific conditions, pulse

compression can approach the TL case making for an optimistic method for substantial pulse compression.

2.5 Group Delay Dispersion

Just as in the field of ultrafast optics, rarely is the solution to a problem a one-step approach where one must only spectrally broaden a pulse for greater time resolution. While broadening a pulses spectrum will yield TL cases of ever short pulses, in practice it also introduces dispersion. If the goal is to compress ultrashort pulses, one must ensure that all frequencies of light from the broadened spectra arrive at a measurement point at the same time. As intense light propagates through a medium and incurs additional frequencies shifting from the central carrier frequency "ω_0", these new wavelengths will travel through the said medium at different velocities. Red shifted frequencies will propagate at a faster rate as compared to those of a blue shifted nature. The total dispersion induced time delay on a pulse is known as group delay dispersion (GDD).

To begin with, we'll consider the spectral phase of our propagating wave as a function of frequency $\phi(\omega)$. By Taylor expanding our phase function depending on frequency we have

$$\varphi(\omega) = \varphi(\omega_0) + \varphi'(\omega_0)(\omega - \omega_0) + \frac{1}{2}\varphi''(\omega_0)(\omega - \omega_0)^2 + \cdots \tag{2.5.1}$$

Expansion of our phase enables us to make a simplified interpretation of which term we are interested in. The first term conveys the phase constant intrinsic to our wave which is of little significance. The second term is referred to as the "group delay time" and measures the time delay of a specific frequency "ω". Following the delay time comes the last term explicitly expressed, group velocity dispersion (GVD) which is a measure of how the group delay time changes across frequencies. Considering the length "L" of the dispersive medium which our

propagating wave travels through we can express group velocity dispersion as group delay dispersion.

$$GDD \cong \frac{d^2\phi}{d\omega^2} \cdot L \tag{2.5.2}$$

If the group delay dispersion is said to be negative $\frac{d^2\phi}{d\omega^2} < 0$, then the pulse is described as positively chirped. This may seem counterintuitive at first, a negative GDD implies that lower frequencies emerge from the dispersive material first. Conversely, if GDD is defined to be positive $\frac{d^2\phi}{d\omega^2} > 0$, then the higher frequencies emerge from the dispersive material first and the pulse is said to be negatively chirped.

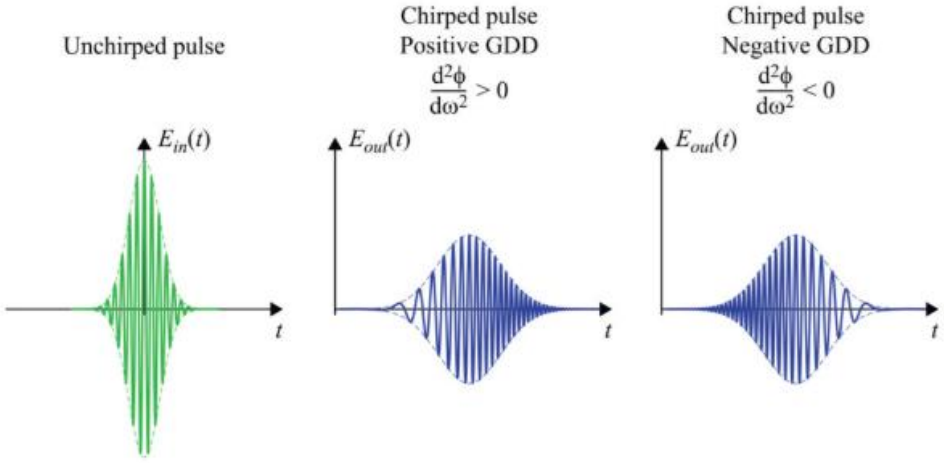

Figure 2.5 Unchirped, negative chirp, and positive chirp pulses. (Source: [15])

2.6 Prism Pair Compressor

In the case of this thesis, the pulse exiting the stretched HCF has negative GDD. Thus, to properly compress our pulse duration from our broadened pulse exiting the HCF, positive GDD must be supplied such that all frequencies of light arrive at the pulse measurement location at the same time.

Prism pair compressors can achieve positive GDD through angular dispersion. Leading lower frequency light encounters the initial prism first is then refracted at the Brewster angle. Higher frequency light while traveling slower through the prism material, will acquire a larger minimal deviation angle compared to the lower frequencies. This difference in minimal angle deviation provides a path length change for the two wavelengths entering the second prism. Emerging from the second prism the wavelengths are collimated and sent back through the prism pair to undo the spatial separation of the differing frequencies acquired on the first pass. Higher frequencies obtain a shorter path length such that when the frequencies spatially overlap after exiting the prism pair, they have obtained positive GDD to offset the negative GDD gained prior [16]. Here β represents the angle between the dispersed wavelengths.

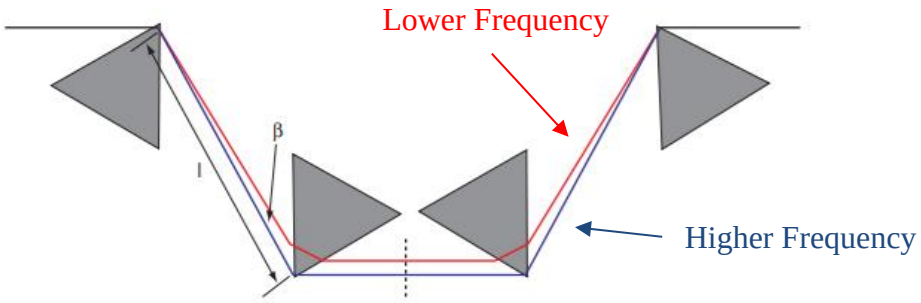

Figure 2.6 Prism Pair arrangement with the dashed line representing a folded arrangement.

2.7 Hollow-Core Fiber Coupling Conditions

When choosing a HCF as the method to broaden spectra, a few considerations must be made to efficiently couple light within the fiber. Core size is arguably the most important parameter as the intensity of the coupled pulse is inversely proportional to the area of the core $I \propto \frac{1}{a^2}$ (a = core radius). Simply put, smaller core fibers allow for more intense beam propagation yielding enhanced nonlinear effects. Furthermore, core size also plays a role in the attenuation

coefficient "α" of a fiber, which may be expressed as a sum of the intrinsic attenuation of a selected fiber, and any bending induced loss

$$\alpha = \alpha_0 + \alpha_R \tag{2.7.1}$$

$$\alpha_0 \propto \frac{\lambda^2}{a^3} \; and \; \alpha_R \propto \frac{1}{\alpha_0 R^2} \tag{2.7.2}$$

where α_0 and α_R represent the intrinsic attenuation of a straight fiber and the additional loss due to bending of the fiber with a radius of curvature "R" [17]. This implies that smaller core fibers inherit greater loss when straight, but experience reduced bending loss compared to larger core fibers.

The intrinsic attenuation of a fiber deserves a more detailed look as the transmission of a HCF is constrained by its length. Stemming from the fact that the gas filled volume of a HCF has an index of refraction less than that of the silica cladding, hollow-core fibers are not index guiding. Rather a HCF guides light through grazing incidence reflection. The attenuation length of a fiber (L_{Loss}^{HCF}) is defined as the where the power confined within the fiber drops to 1/e of its initial value [18]. If we consider a perfectly straight fiber, we may represent the attenuation length as

$$L_{Loss}^{HCF} = \frac{1}{\alpha} \approx 2.4 \frac{a^3}{\lambda^2} \tag{2.7.3}$$

Smaller cored fibers limit the incident angle which a HCF may guide, this lowered incidence angle results in a smaller percentage of light reflected within the fiber as opposed to larger core fibers. Additionally, smaller fibers require more reflections per unit length scaling as $\propto \frac{\lambda}{a}$, accumulating added attenuation. For comparison, at a wavelength of 400nm, a 450μm ID fiber has an attenuation length of ~171m compared to ~1.9m of a 100μm ID fiber. Put another way, the 450μm ID fiber while having a core area 20x larger, grants an attenuation length 90x longer

than the 100μm ID variant before the power transmitted drops to 1/e of the input value. Applying Beer's law to a hollow wave guide of length "L" and transmission coefficient "α", the transmission through the fiber can be described as

$$T = \exp(-\alpha L) \tag{2.7.4}$$

Further consideration to be made concerns the mode coupling conditions. Beer's law accounts for the transmission efficiency once a pulse is coupled within the fiber but neglects modal interference. Thus, we must address how to effectively couple our gaussian single mode pulse (EH_{11}) such that we minimize excitation of other higher ordered modes EH_{1m} (m=2,3,…). For a gaussian beam the hybrid EH modes (electric and magnetic field components) that couple within a hollow-core fiber depend on the relationship between the focal spot diameter and the fiber core diameter. Figure 2.6 showcases the coupling efficiency of the EH_{1m} (m=1,2,3) modes as a function of the focal spot diameter and hollow ID ($\frac{r_0}{a}$).

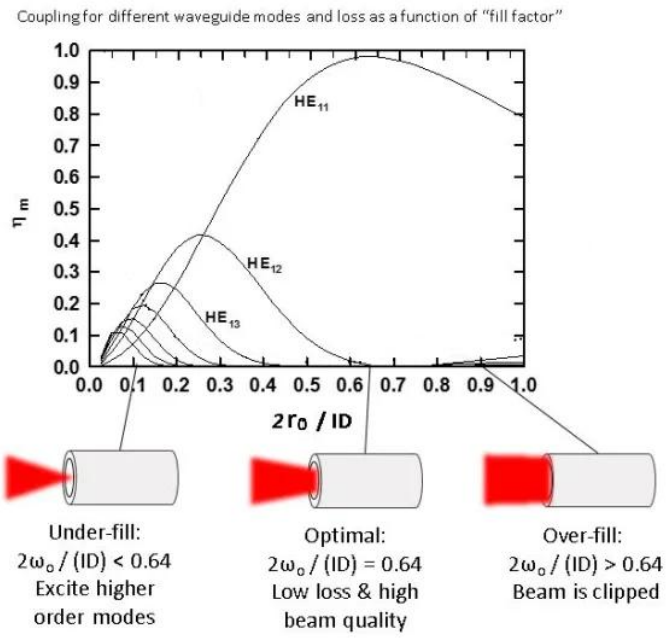

Figure 2.7 EH_{1m} mode coupling efficiency. (Source: [19])

Under proper conditions, coupling into the EH_{11} can reach ~98% with the first higher ordered mode EH_{12} accounting for less than 1% coupled into the fiber. With a focal spot to core radius factor ranging from 0.49 to 0.84, ~90% coupling of the EH_{11} is possible granting greater tolerance to unalterable lab conditions that may constrain achievable focal spot size [20].

2.8 Focal Spot Considerations

Achieving the ideal focal spot size can be accomplished by varying the parameters given in the equation for gaussian beams

$$2r_0 = \frac{4M^2\lambda f}{\pi D} \tag{2.8.1}$$

In the above equation r_0 is the beam waist radius at the focal spot, M^2 is the beam quality factor, λ represents the wavelength, f is the focal length, and D is the beam diameter at the focal lens. For practical consideration, the distance over which the focal spot size remains tightly focused should be considered. Depth of field is a distance over which the focal spot size remains near its minimal focused size relating to the Rayleigh range. A larger depth of field eases the effort of focusing the pulse at the entrance face of the HCF.

$$DOF \approx 2Z_R = \frac{2\pi {r_0}^2}{\lambda} \tag{2.8.2}$$

Another parameter to keep in mind is where exactly the focal spot forms. A gaussian beam's focal spot location may be determined by the simple lens equation

$$\frac{1}{s} + \frac{1}{s''} = \frac{1}{f} \tag{2.8.1}$$

where s, s", and f represent the object distance, image distance, and the focal length. However, in the case of intense light the focal spot may shift depending on the input intensity and material of the medium it propagates through. Thus equation 2.8.1 may be expanded showing the new effective focal length f_{eff},

$$\frac{1}{s}+\frac{1}{s''}+\frac{1}{f_{kerr}}=\frac{1}{f_{eff}} \tag{2.8.2}$$

here f_{kerr} is the nonlinear focal shift, we can further approximate that the "object distance" to be very far away such that $s^{-1} \approx 0$

$$f_{kerr}=\frac{\pi {w_0}^4}{8n_2LP} \tag{2.8.3}$$

$$\frac{1}{s''}+\frac{1}{\frac{\pi {w_0}^4}{8n_2LP}}=\frac{1}{f_{eff}} \tag{2.8.4}$$

where w_0 is the beam waist at the window, n_2 is the nonlinear refractive index of the window material, L is the thickness of the window, and P is the peak pulse power [21].

2.9 Optimal Parameters for 30fs Pulse Generation

Over the course of studying parameters that may generate sub-30fs pulses, there were slight differences between HCF variants. Table 2.9.1 shown below highlights the optimal conditions for generating pulses shorter than 30fs, however, these conditions are not rigid for the generation of short pulses. For example, if less gas pressure is available, higher input energy may compensate for that.

HCF Inner Diameter Core Size (μm)	Fiber Length (cm)	Input Pulse Energy (μJ)	Argon Gas Pressure (psi)	Ideal Focal Spot Size (μm)
100	30	21	20	64
150	70	47	17	96
450	70	200	15	288

Table 2.9.1 Optimal parameters for sub-30fs pulse generation.

CHAPTER 3

EXPERIMENTAL SETUP

This chapter will focus on the commercial laser system supplying our ultrafast 800nm fundamental beam, our custom built second (SHG) and third (THG) harmonic generation setup, the TOPAS OPA to be used in later experiments, HCF setup, prism compression, and transient-grating frequency resolved optical gating (TG-FROG) layout. Additionally, HCF alignment and pressurization techniques are discussed to aid in transmission efficiency of the fiber.

3.1 Laser System Setup

The work presented in this thesis was performed using a femtosecond capable Coherent Inc. laser system. The pump and seed laser system layout shown in figure 3.1.1 captures the pumping, amplification, compressor, SHG UV generation, and lastly the stretched HCF is demonstrated in figure 3.3. A Verdi G5 continuous wave semiconductor laser operating at 532nm outputting 5W is used to pump a MIRA 900 titanium sapphire (Ti:Sa) oscillator. Short pulses are generated within the MIRA through absorbance saturation by Kerr lens mode locking. Output from the MIRA has a nominally 76 MHz repetition rate with a wavelength centered at 800nm, ~130fs pulse duration, ~700mW power and a FWHM bandwidth of ~9.3nm. This output beam is then sent into the Coherent Legend Elite System for amplification.

Within the Legend, there is a high energy Revolution pump laser operating at 527nm, synchronization and delay generator, stretcher and compressor optical grating, Ti:Sa crystal regen cavity, and Pockels cells. Pulses generated from the MIRA are stretched via the optical grating and then sent into the regen cavity to overlap with the Revolution pump laser inside of

the Ti:Sa crystal. Pockels cells allow for the manipulation for the number of round trips within the cavity which determines the amplification. The amplified pulse is then compressed with the optical grating compressor. The result of this process creates an output pulse that is 800nm, ~130fs in duration, a repetition rate of 1KHz, and ~2.8W.

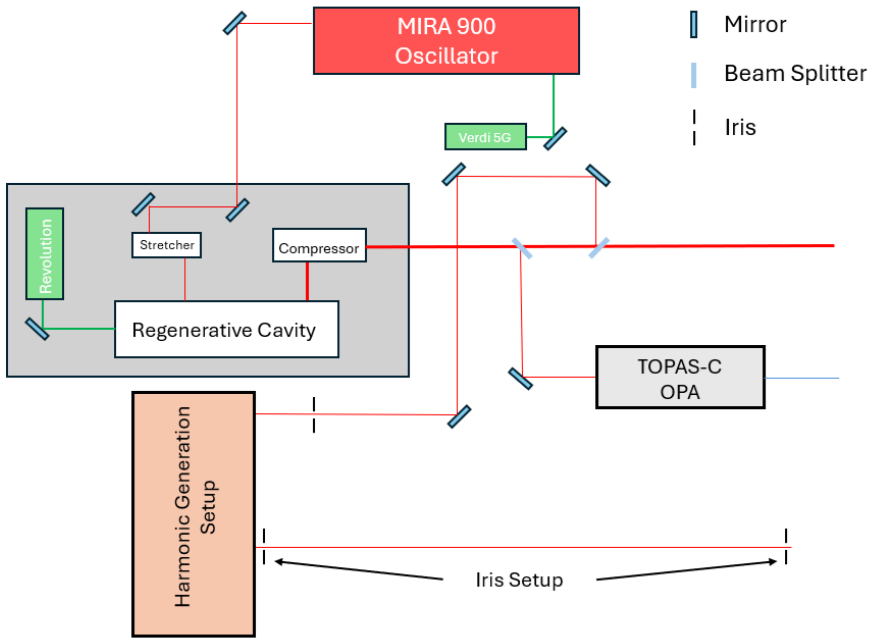

Figure 3.1.1 Laser system setup including harmonic generation setup and TOPAS OPA.

The Legend output beam functions in multiple roles of our lab for varying experimental work. Only a small fraction of the 2.8W output is taken for the stretched hollow-core fiber experiments which is approximately 450mW. The beam is then sent through a circular aperture to modify the beam diameter for later fiber coupling conditions before arriving at our custom-built harmonic generation setup as shown in figure 3.1.2. The 800nm pulse originally has horizontal polarization, upon exiting the SHG BBO generating 400nm, the polarization flips to vertical and lastly returns to a horizontal polarization when exiting the THG BBO crystal as

267nm. The beam at this point is directed towards the HCF setup through a double iris setup for beam collimation.

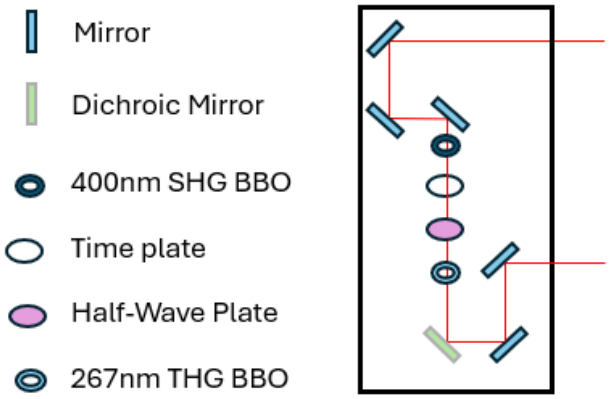

Figure 3.1.2 Custom built SHG and THG setup for 400nm and 267nm generation respectively.

3.2 Fiber Setup

The constructed setup for this thesis is labeled as the “fiber setup”. The design itself is rather straightforward, consisting of a windowed bellow system that is vacuum sealed to hold a pressurized gas of choice.

For functional operation of the HCF system, laser pulses need to be able to enter the setup. KF16 flanges with a 7mm central hole were selected so that a 13mm OD, 2mm thick uncoated CaF2 window could be glued into place. Calcium fluoride windows were chosen to minimize reflection loss at the working wavelengths used (267nm, 400nm, and 800nm). The windows were glued into place using Torr Seal, a two-part epoxy mix resin. After the resin is applied, 24 hours of cure time is given before any pressurization of the fiber can take place. The windows were then O-ring clamped onto a modified NW16 extension fitting. The NW16 extension originally only had a 1/8” NPT thread through one side of the extension such that a

pressure gauge on one end of the fiber could be attached and on the opposing end, a needle valve allowing for the pressurization of the cell.

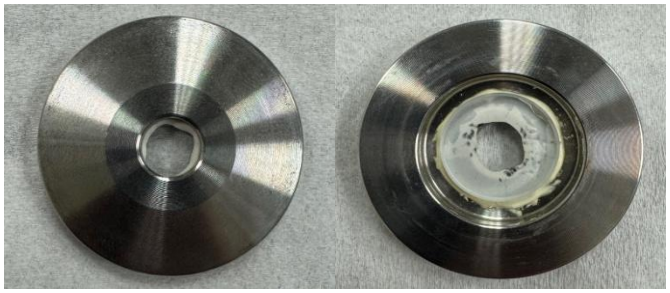

Figure 3.2.1 Front and back view of glued in CaF2 window.

After the resin is applied, 24 hours of cure time is given before any pressurization of the fiber can take place. The windows are then O-ring clamped onto a modified NW16 extension fitting. The NW16 extension originally only had a 1/8” NPT thread through one side of the extension such that a pressure gauge on one end of the fiber could be attached and on the opposing end, a needle valve allowing for the pressurization of the cell. A custom 1/16” drill tap was made underneath each NW16 extension (figure 3.2.2). This smaller drill tap was made so that this NW16 extension can be mounted onto an optical post and was done such that it did not go all the way through the NW16 extension as to avoid gas leakage.

Figure 3.2.2 Custom NW16 extension with 1/16” drill tap.

Custom modified bellows were then attached to both KF16 extensions. Both bellows left one flange untouched such that it can mount onto a KF16 O-ring while the other end had its flange removed and a custom stainless-steel disk welded in its place (figure 3.2.3). This custom bellow disk was 0.75” in outer diameter, 0.25” thick, a 0.25” hole for the fiber to protrude through, as well as four 3/32” threaded holes (figure 3.2.4). Additionally, an O-ring groove was inscribed into the disk to aid in maintaining gas pressure within the cell.

Figure 3.2.3 Custom bellow welded to stainless steel disk.

The custom bellows disk then seals against a custom aluminum disk that will have a fiber glued into it. This fiber disk is 1” in outer diameter, 0.25” thick, a 700µm diameter pinhole drilled through the center, and four 3/32” holes. The specified pinhole size was chosen as the outer diameters of HCF tested ranged from 360µm to 680µm OD. The fiber would then be glued into the pinhole with the Torr Seal epoxy.

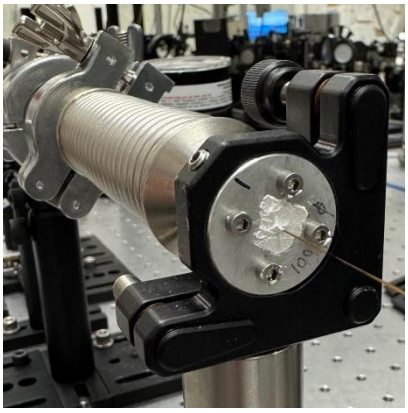

Figure 3.2.4 360µm OD fiber glued into custom aluminum flange.

An OD of 1” for the fiber disk was chosen so that it would mount into a THORLABS 1” mirror mount allowing for tip and tilt adjustments. Additionally, this mirror mount is attached to a 1” OD pedestal pillar post mounted on a THORLABS MDT616 micrometer stage granting fine tuning adjustments in three dimensions. The bellow and fiber disk are then screwed together to form a vacuum tight seal.

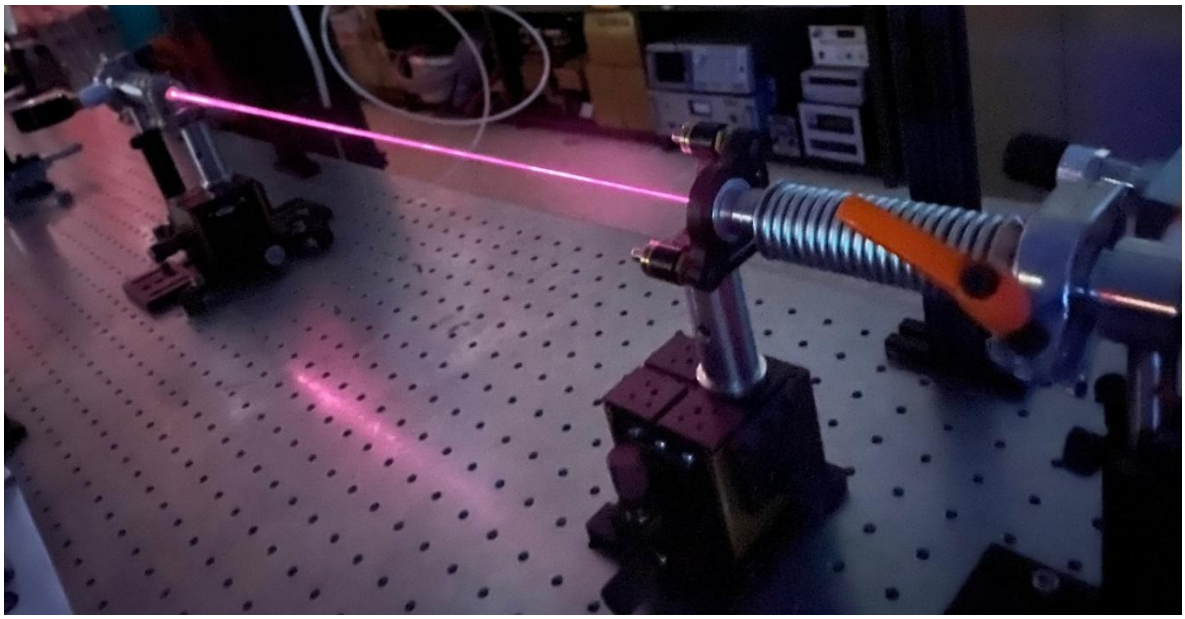

Figure 3.2.5 Stretched HCF setup broadening an 800nm input pulse.

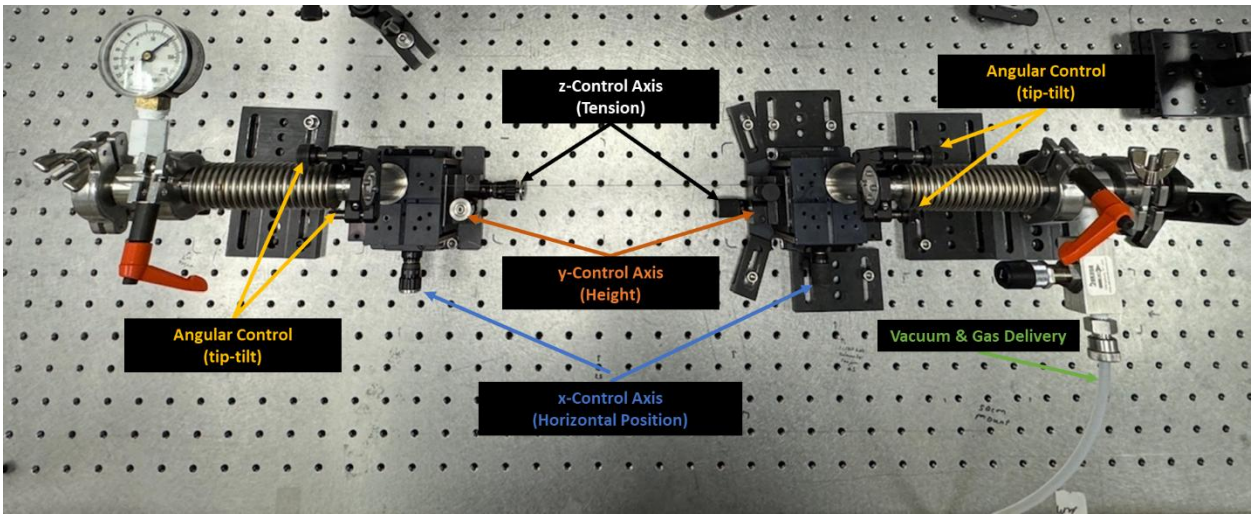

Figure 3.2.6 Micrometer stage and mirror mount controls.

3.3 Beam & Fiber Alignment

A well-planned beam path is critical to establish before attempting to couple light into the HCF setup. A two-iris setup was used with more than 2 meters of separation to ensure no beam path deviation was present. The first iris should be far from the fiber setup with the latter being just a few centimeters in front of the HCF face. With the beam path now established, the fiber mounted on the front and back micrometer stage can be moved into place such that the beam exiting the latter iris hits the fiber face. At this point the bellow system is not attached as it would obstruct your view of where the beam strikes the fiber disk; our goal here is to centralize the beam onto the fiber face. The latter iris can now be removed, and the desired focal lens can be mounted onto a translation stage within the beam path. A density filter prior to the focal lens should be used to avoid any damage while focusing the intense beam in the fiber.

To maximize transmission efficiency, a power meter is placed at the exit end of the fiber. The focal lens will shift the beam slightly and this can be compensated for with both the horizontal and vertical positioning of the micrometer stage, as well as the angular positioning of the fiber relative to the beam with the tip-tilt mirror mount. Tension in the fiber may also be controlled with the micrometer stages; it is recommended to modify tension with the exit end stage as this will not change the front fiber face position relative to the focal spot. Micrometer position, angular control, and tension are all to be used in conjunction to achieve maximum transmission of the input beam. Once transmission efficiency is maximized using the focal lens translation stage, mirror mount tip-tilt, and micrometer stage positioning, the windowed bellows system can be attached to each end of the fiber disks. With the introduction of the CaF_2 window on the input end, the beam path may deviate slightly again from Kerr lensing or slight misalignment of the window inducing refraction. In addition, when the bellows are screwed onto

the fiber disk, the mirror mount can shift as well, potentially changing the original fiber face position. Transmission of the pulse is expected to drop during this phase but should be recoverable following the same procedure listed prior. Once transmission efficiency has been restored, the density filter can be removed or adjusted to allow for the desired input pulse energy to enter the fiber setup.

Upon exiting the HCF, the pulse is divergent and needs to be collimated. A short thin UVFS lens with a focal length of 20cm was placed just outside of the fiber enclosure exit. The collimated beam is now sent through a double pass prism pair compressor to compensate for the positive chirp gained as the pulse traversed the HCF. Lastly, the compressed pulse is picked up with a half-mirror and sent to the TG-FROG apparatus for pulse duration measurements.

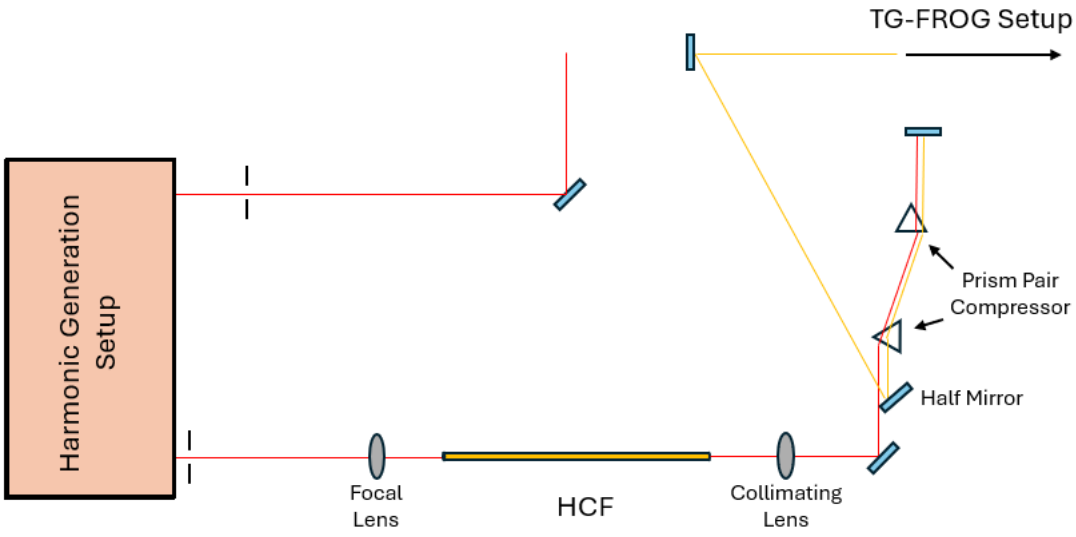

Figure 3.3 HCF and Prism Pair Compressor layout.

3.4 Troubleshooting Fiber Coupling

When coupling light into the HCF, most coupling issues can be resolved through micrometer stage positioning or with the angular adjustment of the tip-tilt mount. However, the input beam can couple into the cladding of the fiber rather than the core which may not be

apparent immediately if only monitoring transmission efficiency or the spectrum of the output pulse. Cladding coupling poses two major issues, the first being that the output beam will form a ring structure (figure 3.4.1) rendering the beam useless when trying to perform pulse duration measurements. Additionally, although the pulse broadens within the cladding as the fiber is now acting as a solid waveguide, it no longer grants the control of the bandwidth broadening as the propagating pulse resides outside of the gas filled core.

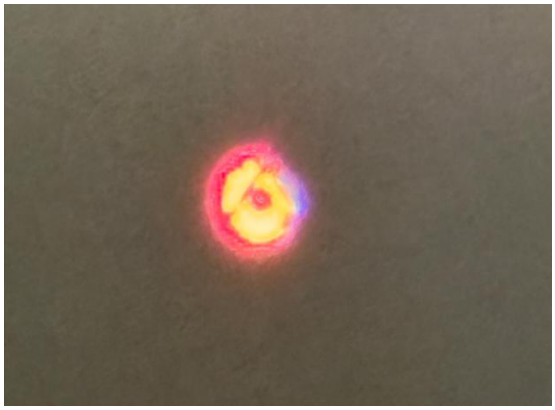

Figure 3.4.1 Input beam coupled into the cladding of a 150μm ID HCF.

The length of the fiber can also impact the transmission efficiency of the HCF as we learned from the attenuation length of a fiber mentioned in the previous chapter. Manufacturing tolerance is a concern as well with inner diameter variation along the length of the fiber potentially leading to mode mixing. With longer lengths of fiber, these imperfections can compound leading to nonuniform beam profiles (figure 3.4.2). Thus, a tradeoff must be made for the shortening of the effective length that spectral broadening can occur for an improved output beam profile (figure 3.4.3). Decreasing the fiber length comes with a few additional benefits aside from an improved beam profile: a smaller footprint within the lab and improved transmission efficiency.

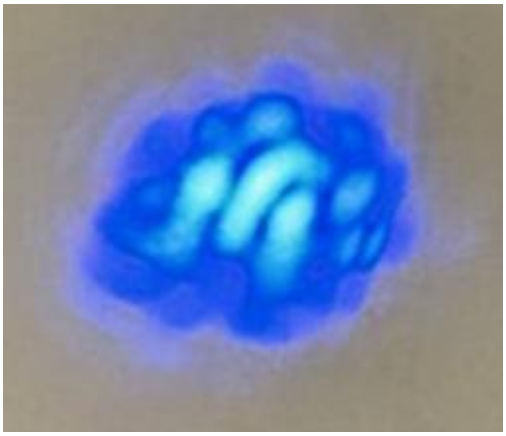

Figure 3.4.2 Non uniform beam profile of a 70cm long 150μm Inner Diameter fiber.

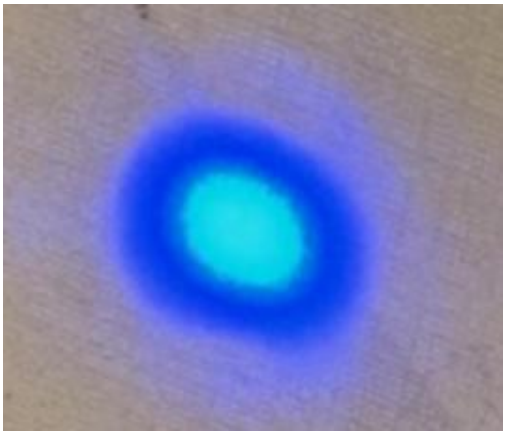

Figure 3.4.3 Uniform beam profile of a 30cm long 150μm Inner Diameter fiber.

3.5 Hollow-Core Fiber Pressurization

Pressurizing the HCF housing is to be done under supervision and with exercised patience. Given that the pressure gauge and gas input are on opposing sides of the stretched HCF, it can take time for the pressure to equilibrate across a length of fiber. This issue is exacerbated by smaller core fibers. While the fiber pressurizes, the mirror mounts the fiber rests on will shift slightly, either reducing or adding tension to the fiber. Too much tension is the primary concern here as the fiber can break under excessive strain. During pressurization one must stay observant of the tension applied on the fiber and use the micrometer stage positioning

to relieve tension as needed. Furthermore, due to the mirror mounts shifting while pressurizing, the fiber position also changes slightly affecting transmission. Changes in transmission can be monitored while pressurizing the stretched HCF enclosure and compensated for during the process and after.

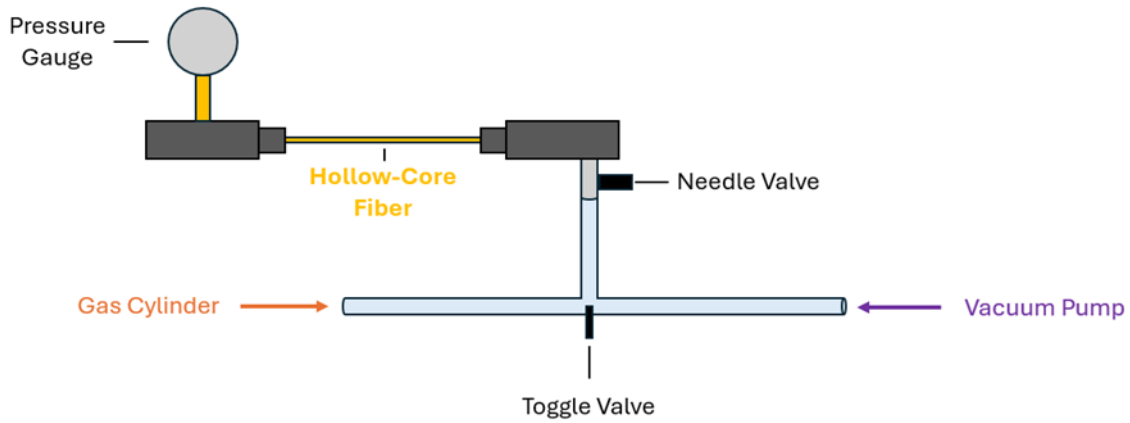

Figure 3.5 Vacuum and gas delivery system to the enclosed stretch HCF.

Initially a vacuum is pumped to -15psi with the needle valve open. This serves the purpose of removing any atmospheric gas that can impinge on the spectral broadening. Once the desired vacuum is reached, the needle valve is closed and either the argon or nitrogen gas cylinder is opened. With the vacuum pump still running, the desired flow rate of gas can be chosen. This can only be done when the vacuum pump is running or the gas line is detached from the fiber system due to the nature of the HCF diameter being so small, the flow rate into the cell will not be distinguishable on the gas cylinder gauge. When the desired pressure is reached, the vacuum process is repeated and filled with gas again. This secondary vacuum and pressurizing of the cell serves to improve the purity of the selected noble gas within the stretched fiber.

3.6 Transient-Grating Frequency Resolved Optical Gating (TG FROG)

Frequency resolved optical gating is a measurement technique that characterizes the time dependent intensity and phase of ultrashort light pulses. There are several methods to carry out FROG experiments that include, polarization gating (PG), second-harmonic generation (SHG), self-diffraction (SD), and transient-grating (TG) that all have various use case advantages. SHG requires the use of nonlinear crystals with strict phase matching requirements. Polarization gratings in the UV tend to be expensive and have the potential to stretch ultrashort pulses that defeat the purpose of the measurement. SD has no need for polarizers, rather, this method generally requires higher energy and does not use a phase-matched interaction meaning that a thin medium for beam overlap is required, complicating the measurement. In this thesis, the approach to compress ultrashort pulses requires a broadened bandwidth which can lower the accuracy of a pulse duration measurement [22]. While TG also relies on phase matching, it is more tolerant to broadened spectra, which is critical for our target of sub-30fs pulses. As a result, the medium where beams overlap occurs can have a longer length.

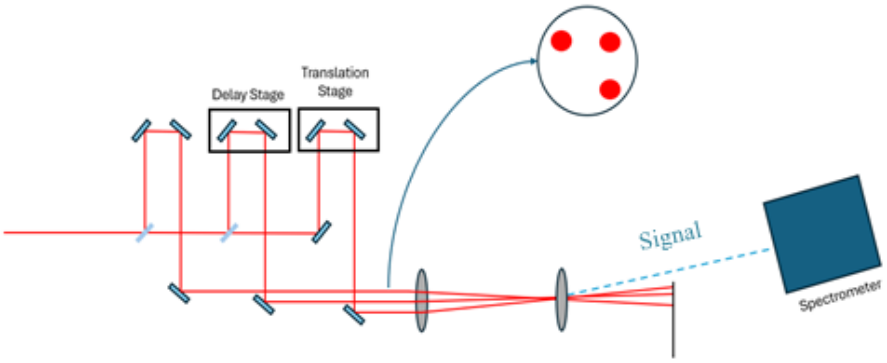

Figure 3.6 TG-FROG Layout.

The general premise of TG-FROG involves splitting the beam of interest into three separate beams. They are to be collimated and run parallel to each other and this is achieved

through sending the transmitted beam through a two-iris setup that are placed before the first and after the second beam splitter. A focusing lens will then focus each beam onto a medium, which in our case is a UVFS plate. To ensure spatial overlap of the three beams, a pinhole is used in place of the UVFS plate. The pinhole is adjusted such that one beam's transmission is maximized and the other two beams are adjusted via their mirror mount for maximum transmission through the pinhole. One of the split beams optical path resides on a fine translation stage. This allows for the control of time delay when this subjected beam reaches the UVFS plate. Once two of the three beams are temporally overlapped, an autocorrelation signal is generated from the UVFS plate. Using an ocean optics HR4000 spectrometer, the signal pulse can be analyzed in fine time delay intervals. The layout of the TG-FROG setup is demonstrated below in figure 3.5.

For analysis of the measured pulse duration, phase retrieval software written in MATLAB is used [23]. The FROG software measures the spectrum of the signal pulse at each delay point and generates a retrieved electric field. Through an iterative process, the FROG algorithm minimizes the difference between the experimental and retrieved traces to produce a defined pulse duration.

CHAPTER 4

EXPERIMENTAL RESULTS AND CHARACTERIZATION

During the investigation of sub-30fs pulse generation in both the UV and DUV, spectral broadening experiments were carried out at 800nm, 400nm, and 267nm wavelengths. The nominal pulse duration used was ~130fs for the entirety of this study. Initial relationships between pulse energy and gas pressure effect on spectral bandwidth were investigated in the near IR to determine feasibility of short pulse generation. Varying HCF core sizes of 450μm, 150μm, and 100μm inner diameters were also investigated. Pulse compression work was later performed for the two shorter wavelengths, 400nm and 267nm. Moreover, long term stability as well as energy and pressure effect on compressed pulse lengths were studied at 267nm. The UV range is our primary interest as our lab studies excitation dynamics of molecules which exhibit strong absorption in this wavelength range.

4.1 Input Energy and Gas Pressure Effects on the Transform Limit

Preliminary work was carried out to understand the impact that both input pulse energy and nitrogen gas pressure have on bandwidth broadening for later UV pulse compression. A 70cm, 450μm inner diameter fiber was the first HCF selected to use. A relatively large core diameter was selected first to minimize the difficulty of effectively coupling the input beam into the fiber. Pulse energies ranging from 100μJ to 350μJ with a central wavelength of 800nm were launched into the HCF prior to the addition of the gas cell (Figure 4.1.1). As expected, increasing pulse energy led to broadening of the pulse bandwidth, the most energetic case of 350μJ corresponds to a transform-limited (TL) pulse duration of ~30fs. While promising, a transform-

limited pulse duration is not practical to achieve. Furthermore, the UV output available from our TOPAS setup that this fiber was designed to use will have far less pulse energy to work with.

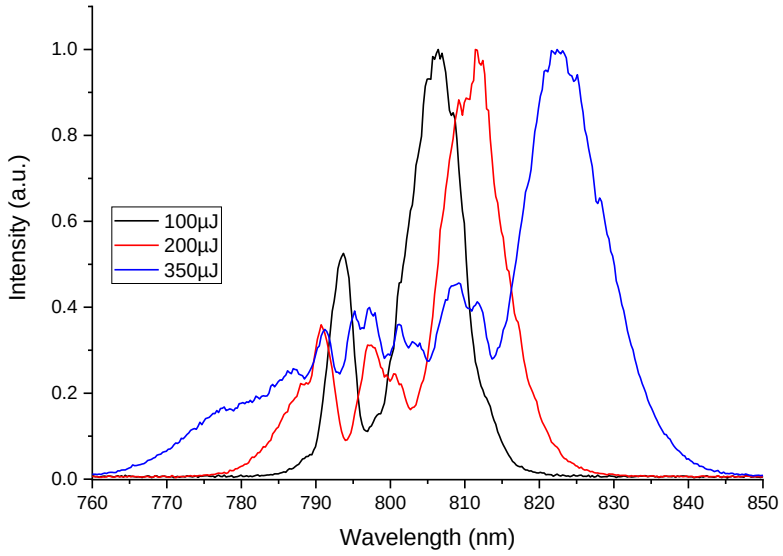

Figure 4.1.1 Broadened spectrum output of 450μm ID HCF at atmosphere.

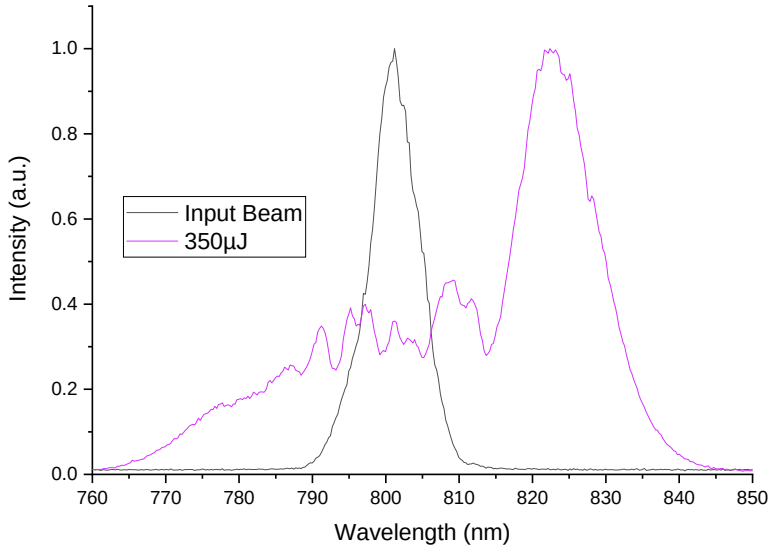

Figure 4.1.2 Bandwidth comparison between input beam and maximum input energy.

The next logical step was determining how much additional bandwidth can be obtained by pressurizing the gas cell. A consequence of the gas cell is that the CaF_2 windows placed in front and back of the fiber have ~85% transmission. Thus, in pressurized experiments, the input pulse energy entering the fiber ranged from 100µJ to 300µJ and generated FWHM spectra of 13.8nm to 60.57nm (figure 4.1.3).

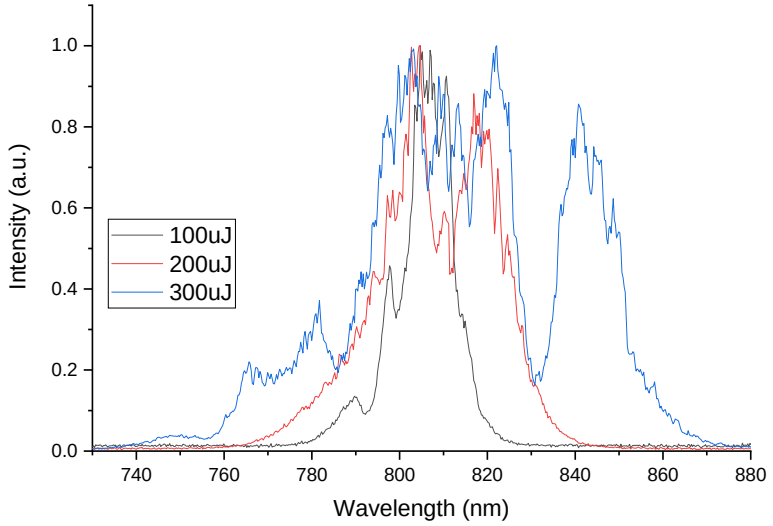

Figure 4.1.3 450µm fiber spectral broadening at 15psi nitrogen pressurization.

Energies exceeding 200µJ generated broadened spectrums with a transform-limited pulse duration of sub-30fs and at the maximum case of 300µJ, TL pulse duration was as low as ~16fs. Such low TL pulse durations offer a promising sign as in practice, the compressed pulses cannot physically realize their lowest transform-limited case. Therefore, shorter transform-limited pulses grant more leniency achieving the targeted sub-30fs pulse. Actual pulse duration measurements are left to the UV region wavelengths of 400nm and 267nm as the TG-FROG setup houses mirrors and beamsplitters designed for UV work.

4.2 400nm Spectral Broadening

With the promise of sub-30fs pulses appearing achievable, the next step was to transition to UV pulses by modifying our input 800nm beam with a frequency doubling BBO crystal. Future experimental work making use of the stretched HCF will utilize our TOPAS setup which can generate wavelengths down to the DUV. Consequently, the TOPAS is constrained to low energy pulses compared to what the Coherent Legend system produces, with 50µJ pulse outputs being a maximal scenario. Thus, a density filter was placed prior to the gas cell in our fundamental beam pathway to mimic the TOPAS energy output of no more than 50µJ. This low energy constraint proved problematic when measuring the output pulse at both atmospheric conditions and when pressurized with 15psi of nitrogen gas (figure 4.2.1).

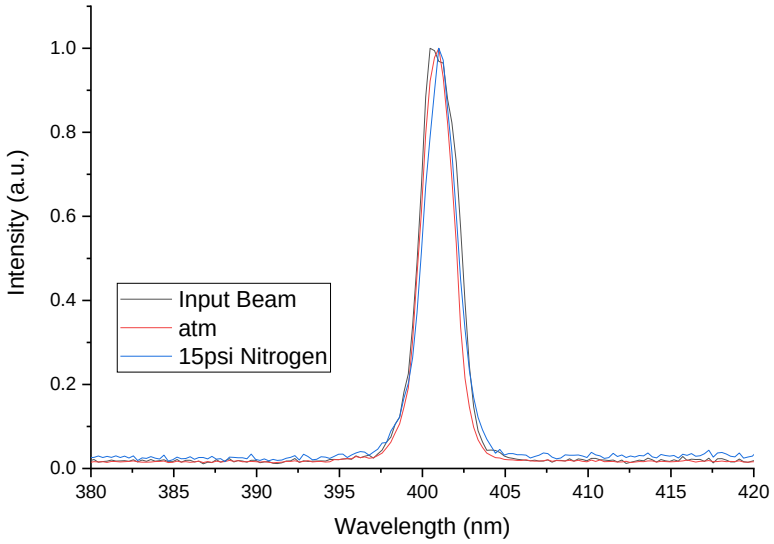

Figure 4.2.1 450µm ID fiber spectra output from 47µJ input energy compared to the input beam.

The output pulse appears indistinguishable from the reference input beam with no noticeable bandwidth increase. These results paint a pessimistic outlook as future experimental work will be constrained to this low energy regime where a 450µm ID fiber does not confine

light intense enough to illicit a strong nonlinear response. Even at high pressure setting of 15psi, virtually no spectral bandwidth was observed.

Thus, the decision was made to go to a smaller 150µm inner diameter HCF that was similar in length (70cm) to that of the 450µm ID fiber. As intensity is inversely proportional to area, this reduction of core size to 150µm provides a factor of 9x increase in intensity for the duration of propagation within the fiber. Figure 4.2.2 shown below compares the two different core size fibers 450µm and 150µm, that produced a FWHM of 2.43nm and 11.32nm respectively at 15psi of nitrogen pressure.

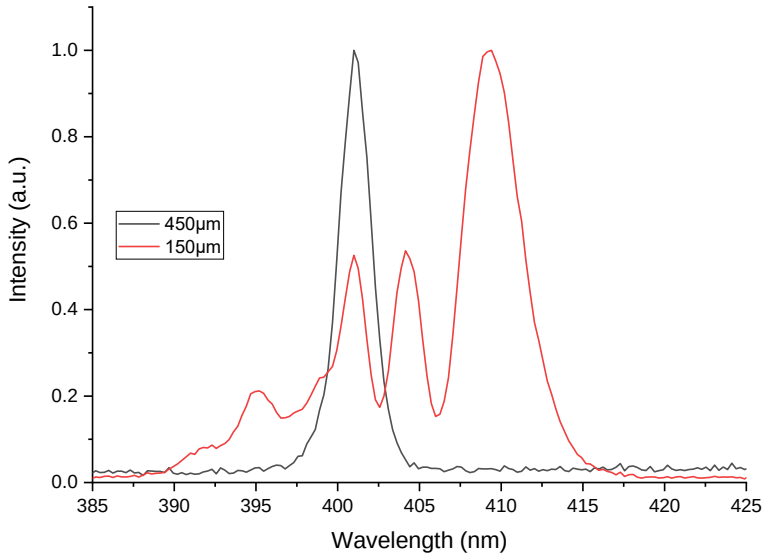

Figure 4.2.2 Spectral broadening seen between two 70cm length HCF of 150µm and 450µm core diameters at 47µJ input energy and 15psi of nitrogen.

This corresponds to a TL pulse duration of 97.8fs (450µm) and 21.6fs (150µm), a reduction factor of 4.5x in pulse duration. Further work was done investigating how argon would compare to nitrogen in generation of broadened bandwidths within the 150µm HCF. Comparable broadening was found between the two gases at both low and high pressure (figure 4.2.3 and

4.2.4). Nitrogen showcased an affinity to have its central wavelength redshift opposed to argon that spectrally broadened more uniformly around its central wavelength.

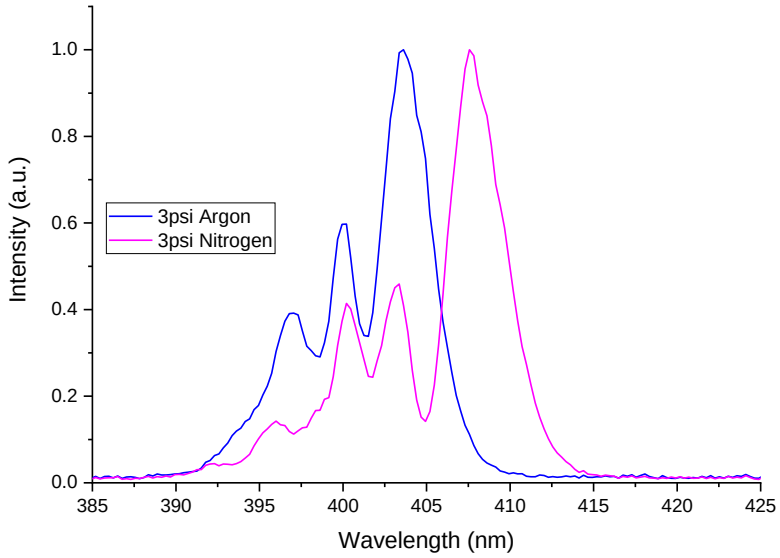

Figure 4.2.3 Low pressure comparison of nitrogen and argon in a 70cm length 150µm fiber.

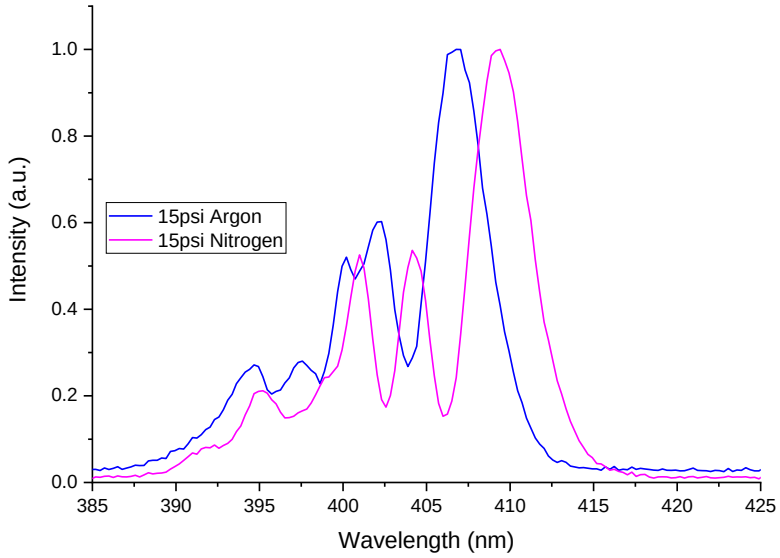

Figure 4.2.4 High pressure comparison of nitrogen and argon in a 70cm length 150µm fiber.

Argon was selected as the preferred gas of choice at this point as compression of a symmetrically broadened pulse around its central wavelength is easier in practice to perform than that of a pulse experiencing more asymmetrical red shift. Although this transition to a smaller core size yields favorable bandwidth broadening, the transmitted beam showcased a poor beam profile.

As was mentioned earlier in chapters 2.7 and 3.4, focal spot size mismatch to the fiber core or imperfections in core size and structure along the length of fiber can result in higher-ordered modes being generated, deteriorating the output beam profile as well as making it difficult to characterize. Length of the 150µm fiber was suspected as the cause of the beam profile seen in figure 3.4.2; however, shortening fiber length decreases the effective length over which self-phase modulation occurs which produces the widened bandwidths. A compromise was selected where a smaller ID fiber of 100µm was chosen with a length of 30cm, which was compared against the 70cm long 150µm variant show in figure 4.2.5 below.

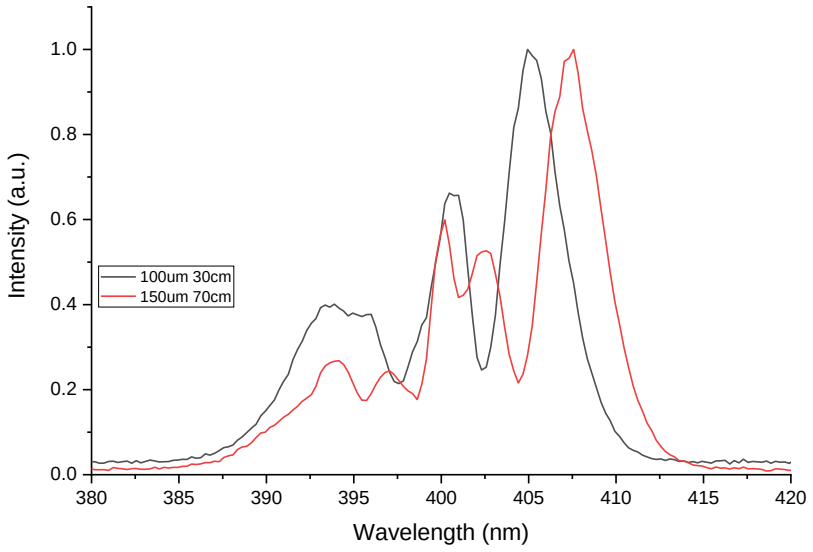

Figure 4.2.5 13.7nm and 12.7nm FWHM bandwidth of 100µm and 150µm fiber respectively (47µJ input energy at 17psi of nitrogen).

Although the effective length is just ~43% of the previous fibers, the decreased core size allows for intensities greater than 2x and 20x that of the 150µm and 450µm fibers respectively. At 17psi argon pressurization, the shorter and smaller ID 100µm fiber produced a larger bandwidth of 13.7nm with a TL pulse duration of ~17fs compared to 12.7nm and 19fs of the 150µm fiber.

4.3 400nm Pulse Compression

The broadened spectra of the 100µm inner diameter fiber were compressed by utilizing a pair of ultraviolet fused silica prism compressors. Energy input into the fiber at this point had dropped to 37µJ resulting from issues with the Coherent laser system at the time. In an effort to counterbalance the reduction in laser output energy, pressurization was pushed near the maximum limit of 20psi argon gas within the stretched HCF setup. To this point, no spectral bandwidth broadening limit has been observed for either input pulse energy or gas pressurization.

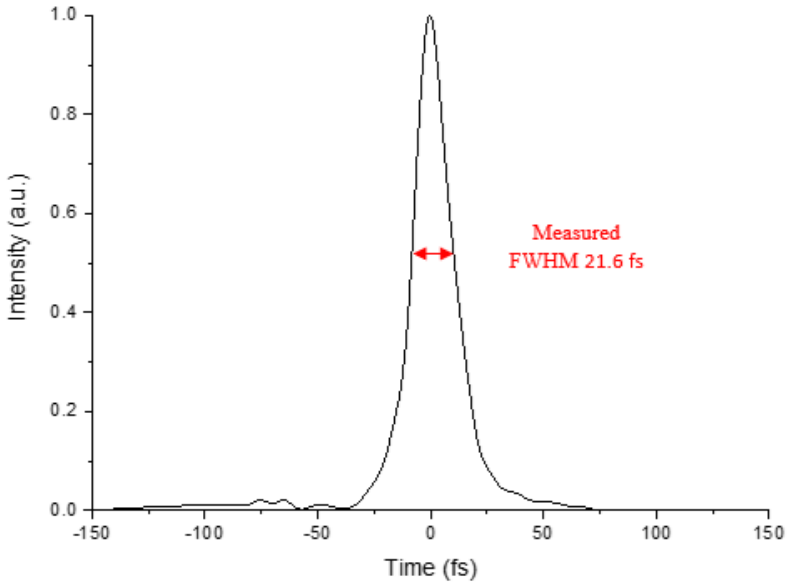

Figure 4.3.1 21.6fs TG-FROG measured pulse at 37µJ input energy and 20psi argon.

The prism pair tip distance was tuned experimentally to generate the shortest possible pulse at 50cm tip-to-tip separation. Under these optimal conditions, a TG-FROG measured pulse was recorded at 21.6fs shown in figure 4.3.1.

4.4 267nm Spectral Broadening

The ultimate goal of this work was to generate sub-30fs pulses in the deep ultraviolet range, specifically at 267 nm. Spectral broadening was compared for the 100µm ID fiber at 21µJ input pulses (figure 4.4.1). Less energy is present at 267nm due to the strict phase matching nature that triple harmonic generation requires. At this lower energy, 15psi argon broadens the bandwidth to a TL pulse duration of 31.5fs making it nonviable for sub-30fs generation. However, at the upper pressure limit capable within the gas cell, 20psi of argon gas produced bandwidths that are well under the TL 30fs limit with 19.8fs pulse duration theoretically possible.

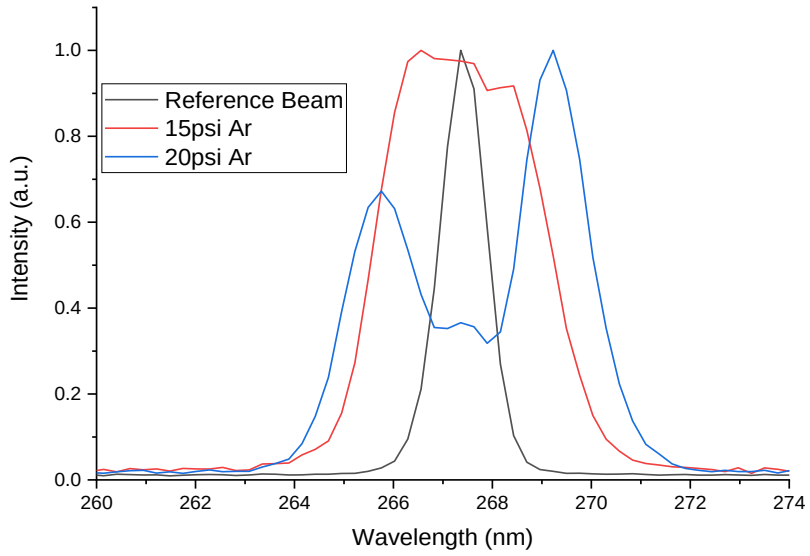

Figure 4.4.1 21µJ input pulse energy spectral broadening comparison between argon at 15 and 20psi.

4.5 267nm Pulse Compression

With sufficient broadening conditions seen in section 4.4, we have reached the final stage in achieving the generation of sub-30fs pulses in the deep UV, namely 267nm. With an input pulse energy of 21μJ and prism tip-to-tip distance optimized at 20.5cm of separation, pulses were measured as low as 24.1fs!

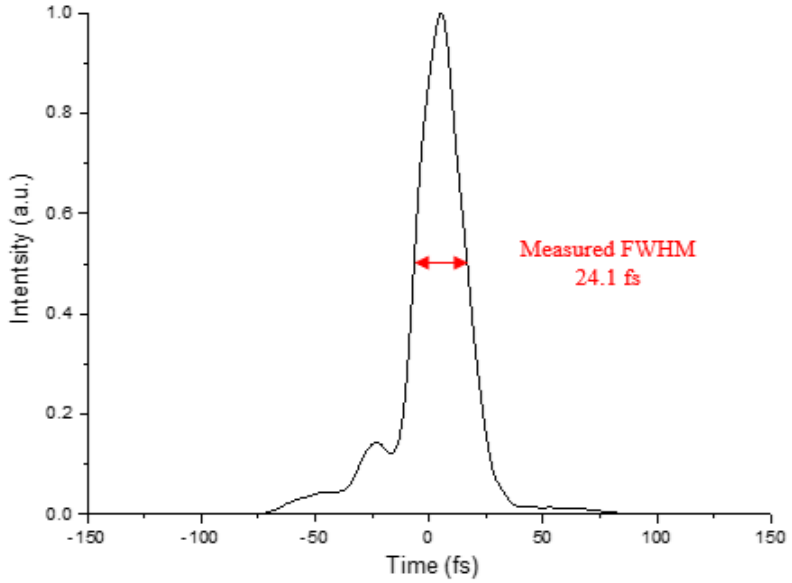

Figure 4.5.1 24.1fs TG-FROG measured pulse at 21μJ input energy and 20psi argon.

4.6 Experimental Validation of Fiber Setup for TRPES Applications

With sub-30fs pulses demonstrated, further work was performed to validate the HCF system for future time resolved photoelectron spectroscopy experiments (TRPES). Namely the impact that input pulse energy and argon pressure have on the measured pulse duration, as well as the long-term stability of the setup.

Optimal pulse compression was performed for a range of input energies spanning from 10-27μJ with the gas cell argon pressure set to the upper limit of 20psi. At lower pulse energy input, pulse compression approaches more closely to the Fourier transform limit.

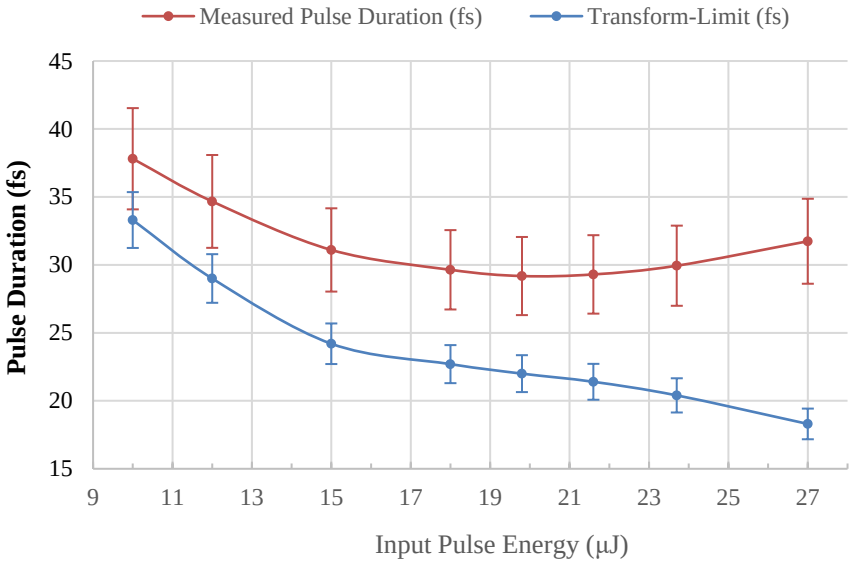

Figure 4.6.1 Energy Dependence on measured pulse duration at optimized prism tip separation.

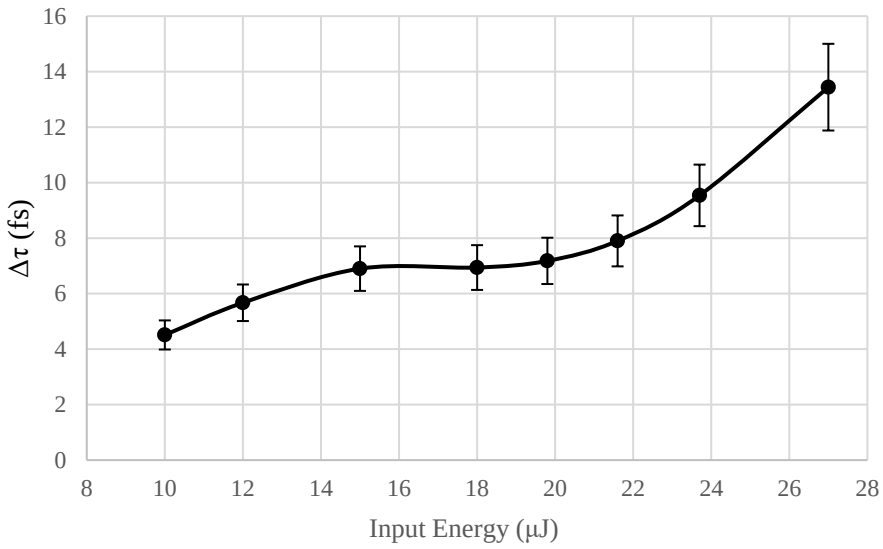

Figure 4.6.2 Difference between measured pulse duration and transform limit.

Maximal pulse compression is limited beyond 20μJ input energy from potential nonlinear effects such as two photon absorption within the fused silica prisms inducing self-focusing [24].

Additionally, pulse compression becomes much harder to characterize and optimize at shorter time durations. This can be explained due to the nature of TG-FROG relying on spectral phase matching conditions which becomes increasingly difficult to satisfy as the spectral bandwidth broadens.

The effect of input pulse energy at a fixed prism-tip distance was performed to profile the variation on compressed pulse duration at varying energies. At a maximum argon pressure of 20psi, the input pulse energy again ranged from 10-27μJ. The measured bandwidths produce transform-limit durations from 33.3fs to as low as 18.3fs. Energy input as low as 15μJ yields sufficient broadening to allow for sub-30fs pulse compression. With a transform limit of 23.2 fs, there is sufficient margin to reliably achieve a measurable pulse duration on the order of 30 fs. However, the compressed pulse duration is highly sensitive to the input pulse energy, requiring careful adjustment of the prism compressor's tip-to-tip distance for any deviation of pulse energy the prism compressor was originally optimized for.

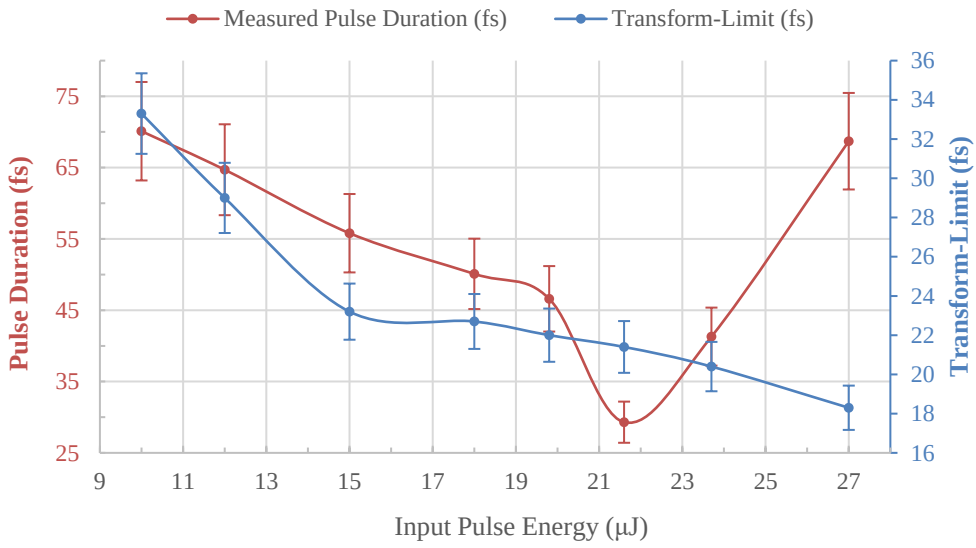

Figure 4.6.3 Energy dependence on measured pulse duration at 20.5 cm prism tip separation and 20 psi argon pressure.

Input pulse energy was then fixed at 21.6μJ and the argon pressure varied from 3psi to the upper limit of 20psi. At this input pulse energy, pressures greater than 17psi are required to generate bandwidths suitable for realizable sub-30fs compression.

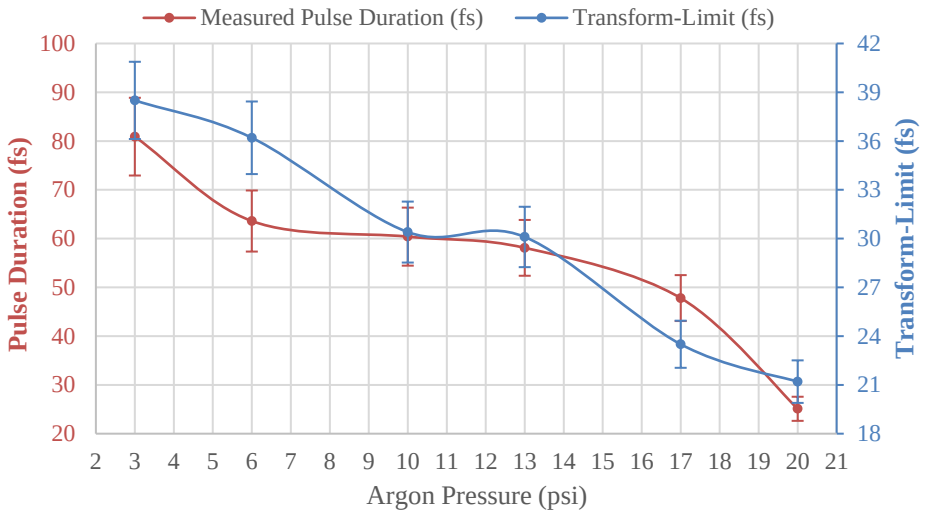

Figure 4.6.4 Pressure Dependence on measured pulse duration at a fixed prism distance of 20.5cm and energy input of 21.6μJ.

The studies of energy and pressure dependence at a fixed prism tip distance serves as a realistic view of how this system will behave when generating compressed pulses. While the system experienced no noticeable pressure leakage over the course of several weeks, laser power output from the Coherent system does vary. Thus, the energy input entering the fiber must always be known and adjusted as needed. Alternatively, the prism compressor distance can be adjusted but generally this is more difficult in practice.

Lastly, a long-term stability test was conducted over 7 hours with a fixed input energy of 23μJ and prism tip separation remaining at 20.5cm (figure 4.6.3). Over this time, 42fs was the maximum pulse duration measured, 30fs was the shortest duration, and the average pulse duration reported was 36.3fs. Note that the input pulse energy was slightly elevated from the

21.6μJ pulse which the prism tip separation was optimized for. As a result, the average pulse duration was measured to be just above the 30fs limit.

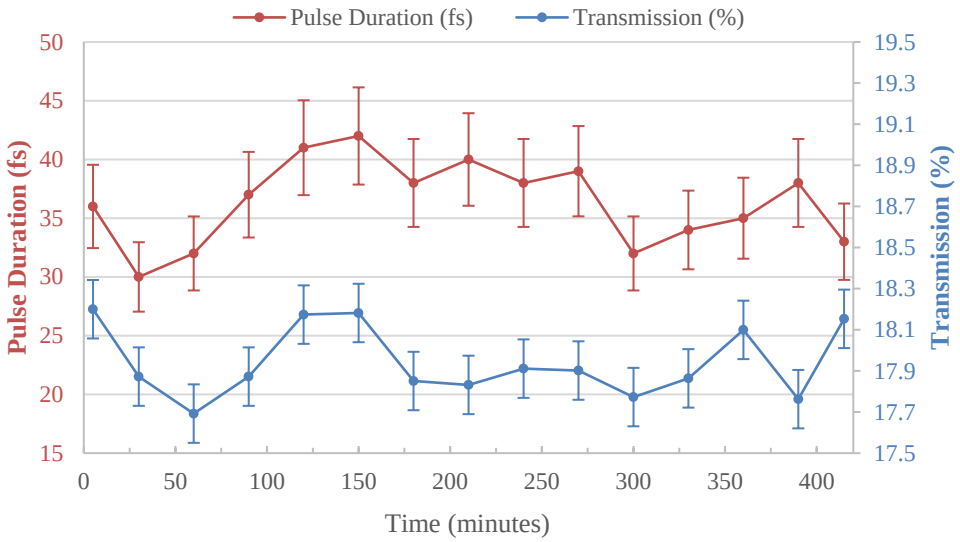

Figure 4.6.5 Stability test at a fixed prism distance of 20.5cm, 20psi of argon, and input energy of 23μJ.

CHAPTER 5

SUMMARY AND OUTLOOK

The goal of this project was to create a low cost, easy to tune hollow-core fiber setup that would yield sufficient spectral broadening for post compression of sub-30 femtosecond pulses in the ultraviolet range. Several fiber core size variants were tested with the 30cm 100μm ID core variant proving feasible for temporal pulses lower than 25fs at both 400nm and 267nm while maintaining a uniform transmitted beam profile. While exceptionally sensitive to beam pointing within the fiber, the setup proved to be stable over prolonged use once the input pulse coupling is optimized.

Argon was determined as the preferred gas of choice due to the broadening nature maintaining a more symmetric bandwidth profile than that of nitrogen which displayed a more asymmetrical red-shift profile. Input pulse energies as low as 15μJ provide sufficient broadening for realizable sub-30fs pulse duration. Although pulse energies >21μJ begin to show adverse temporal trends, no adverse effects of argon pressure have been observed.

Future improvements to be made are the replacement of UVFS focal and collimating lenses that reflect about ~15% of the 267nm beam. In the case of reduced supplied laser power, this lens replacement may afford sufficient input and output pulse energies. Additionally, the replacement of the UVFS thin collimating lens and prism compressor for an alternative CaF_2 medium would allow for improved compression in the deep UV. Moreover, a more secure method of window application to the gas cell may allow pressures within the system to go beyond the 20psi limit I experienced. Increased argon pressure may allow for less pulse energy

needed for sufficient spectral bandwidth broadening resulting in diminished effects of nonlinear processes within fused silica materials within deep ultraviolet frequencies.

For further time resolution, the hollow-core fiber setup may be used in a cascaded setup such that the broadened spectrum from the first fiber is sent to a second fiber for further broadening assuming that pulse intensity remains sufficiently high after transmission. This technique will require more energetic pulses as the transmission loss is cumulative. A cascade self-phase modulation setup of the fiber setup described in this thesis would allow for further enhanced time resolution.

With the feasibility of such short pulse durations demonstrated and long-term stability established, this setup will be exceptionally valuable for studying ultrafast dynamics and molecular vibrational coherences. Material science research, particularly in nanomaterials and semiconductors, will benefit from improved understanding of electron-phonon dynamics [25]. Additionally, biological and chemical studies will gain from enhanced time resolution, offering deeper insights into energy transfer in complex molecules [26]. These are just a few of the many fields that would benefit; others, such as quantum technologies, plasma physics, energy research, and photonics, would also see significant advancements.

As was mentioned in the introduction, the HCF may even serve as a tool for wavelength tuning, potentially removing the need for certain expensive nonlinear crystals use in optical parametric amplification. Depending on the application, an OPA may even be deemed fully replaceable by this low-cost alternative!

REFERENCES

[1] Poisson, L., Lépine, F. Ultrafast phenomena from attosecond to picosecond timescales: theory and experiments. Eur. Phys. J. Spec. Top. 232, 1995–2000 (2023).

[2] Zürch, M., Chang, HT., Borja, L. et al. Direct and simultaneous observation of ultrafast electron and hole dynamics in germanium. Nat Commun 8, 15734 (2017).

[3] Leahy-Hoppa M.R., Miragliotta J., Osiander R., Burnett J., Dikmelik Y., McEnnis C., Spicer J.B. Ultrafast laser-based spectroscopy and sensing: applications in LIBS, CARS, and THz spectroscopy. Sensors. (2010).

[4] J. Kasparian, J.-P. Wolf Ultrafast laser spectroscopy and control of atmospheric aerosols Phys. Chem. Chem. Phys., 14 (26) (2012), pp. 9291-9300.

[5] Warren, W. Ahmed Hassan Zewail (1946–2016). Nature 537, 168 (2016).

[6] D. Faccio, A. Grün, P. Bates, O. Chalus, and J. Biegert, "Optical amplification in the near-infrared in gas-filled hollow-core fibers," Opt. Lett. 34, 2918-2920 (2009).

[7] "Paraxial Wave Equation and Gaussian Beams." Fundamentals of Photonics: Quantum Electronics, MIT OpenCourseWare, Massachusetts Institute of Technology, Spring 2006, https://ocw.mit.edu/courses/6-974-fundamentals-of-photonics-quantum-electronics-spring-2006/871c32e6e4a44cbb1546741ef06f0f2f_parax_wav_eq_gau.pdf.

[8] Moreno, Michelle. “Kerr Effect.” Instituto de Física de São Carlos, Universidade de São Paulo, June 14, 2018.

[9] Choudhary, S., & Boyd, R. W. “Tutorial on Nonlinear Optics.” Proceedings of the International School of Physics “Enrico Fermi” Course 190 “Frontiers in Modern

Optics", edited by D. Faccio, J. Dudley, and M. Clerici, IOS, Amsterdam; SIF, Bologna, 2016, pp. 31-74. DOI: 10.3254/978-1-61499-647-7-31.

[10] University of Central Florida. "Lecture 18: Self-focusing, Self-phase Modulation, Spectral Broadening, and Supercontinuum Generation." University of Central Florida, 2023.

[11] Mohammed, Nazmi & Ragab, Mahmoud & Aly, Moustafa. (2012). Self-Phase Modulation Based Wavelength Conversion using Different Types of Fibers. European Journal of Scientific Research. 74. 1450-216.

[12] Tamas Nagy , Peter Simon & Laszlo Veisz (2021) High-energy few cycle pulses: post-compression techniques, Advances in Physics: X, 6:1, 1845795, DOI: 10.1080/23746149.2020.1845795

[13] Börzsönyi, Á., Heiner, Z., Kovács, A. P., Kalashnikov, M. P., & Osvay, K. "Measurement of Pressure Dependent Nonlinear Refractive Index of Inert Gases." Optics Express, vol. 18, no. 25, 2010, pp. 25847-25854. DOI: 10.1364/OE.18.025847.

[14] Paschotta, R. "Time–bandwidth Product." RP Photonics Encyclopedia, RP Photonics AG, 2023. DOI: 10.61835/bfb.

[15] Plymouth Grating Laboratory. "Figure 7: Illustration of Unchirped and Chirped Pulses." PGL Technical Note – Dispersion and Pulses, Plymouth Grating Laboratory, 2025.

[16] Newport Corporation, "Prism compressor for ultrashort laser pulses," Application Note 29, Accessed: Feb. 24, 2025. [Online]. Available:

https://www.newport.com.cn/medias/sys_master/images/images/hfb/hdd/9520061349918/DS-11065-Apps-Note-29-new-temp.pdf

[17] Nagy, T., Simon, P., & Veisz, L. (2020). High-energy few-cycle pulses: post-compression techniques. Advances in Physics: X, 6(1). https://doi.org/10.1080/23746149.2020.1845795

[18] Travers, J. C. “Optical Solitons in Hollow-Core Fibres.” Optics Communications, vol. 555, 2024, p. 130191. DOI: 10.1016/j.optcom.2023.130191.

[19] Nubling, R. K., & Harrington, J. A. “Launch Conditions and Mode Coupling in Hollow-Glass Waveguides.” Optical Engineering, vol. 37, no. 9, 1998. DOI: 10.1117/1.601768.

[20] Nisoli, M., Stagira, S., De Silvestri, S., Svelto, O., Sartania, S., Cheng, Z., Tempea, G., Spielmann, C., & Krausz, F. “Toward a Terawatt-Scale Sub-10-fs Laser Technology.” IEEE Journal of Selected Topics in Quantum Electronics, vol. 4, no. 2, 1998, pp. 414-419. DOI: 10.1109/2944.668741.

[21] C. Brahms, "The effect of nonlinear lensing on the coupling of ultrafast laser pulses to hollow-core waveguides," Optics Express, vol. 31, no. 5, p. 7187, 2023. doi: 10.1364/oe.482749.

[22] John N. Sweetser, David N. Fittinghoff, and Rick Trebino, "Transient-grating frequency-resolved optical gating," Opt. Lett. 22, 519-521 (1997).

[23] Trebino, Rick. (2000). Frequency-Resolved Optical Gating: The Measurement of Ultrashort Laser Pulses. 10.1007/978-1-4615-1181-6_6.

[24] Kinyaevskiy, I.O., Koribut, A.V., Danilov, P.A. et al. Self-Focusing and Self-Phase Modulation of a Focused Femtosecond Laser Beam in Fused Silica at Near-Critical Peak Power. Jetp Lett. 119, 10–15 (2024). https://doi.org/10.1134/S0021364023603585.

[25] Kopp, J. (2021, September 16). Enhancing Semiconductor Fault Isolation With Time-resolved Laser-assisted Device Alteration. Thermo Fisher Scientific. Retrieved from https://www.thermofisher.com/blog/semiconductors/enhancing-semiconductor-fault-isolation-laser-assisted-device-alteration/

[26] Liang, K., Bi, L., Zhu, Q., Zhou, H., & Li, S. (2023). Ultrafast dynamics revealed with time-resolved scanning tunneling microscopy: A review. ACS Applied Optical Materials, 5(5), 1401–1416. https://doi.org/10.1021/acsaom.2c00169

APPENDIX A

FIBER CLEAVING

Achieving a clean cleave on both ends of the fiber is paramount to creating a suitable HCF for pulse compression covered in this thesis. If a poorly cleaved fiber were to be used various issues may arise including poor transmission, nonuniform beam output profile, and mitigated spectral broadening to name a few. While both ends need a clean cleave, the better end should be used as the pulse input side. This is because the quality of the output beam profile depends heavily on how the pulse is coupled into the HCF. Below lists a general procedure for the cleaving of a HCF (the same process was used for all fiber variants mentioned within this thesis).

Procedure:

1. Prior to cutting the fiber, determine the length of fiber you want to work with. Allow yourself several additional centimeters of length on both ends as the first cleave isn't always sufficient.
2. Straighten out the fiber on a hard flat surface and press down on one end with a free hand such that it cannot move. Apply the cleaving tool on top of the fiber coating at a ~30-degree angle as shown below.

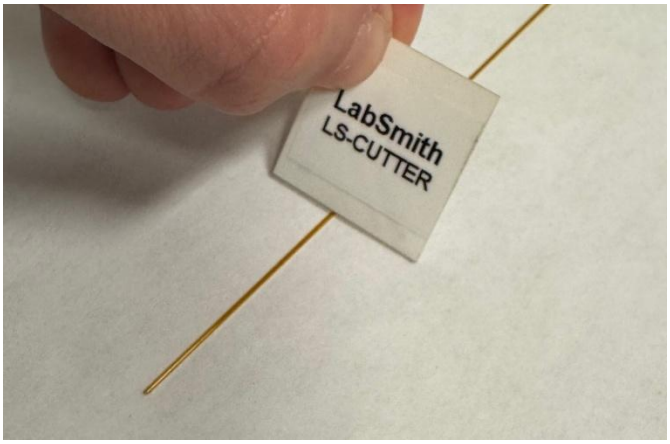

3. Press the cleaving tool into the cladding at the ~30-dgree angle while pulling gently on the fiber with the hand previously used to press the fiber down away from the cleaving tool. The goal here is **not** to press the cleaving tool through the cladding and glass.
4. If done correctly, the fiber at first will look unchanged. At the point you applied the cleaving tool, you can now bend that segment of fiber and it should fall of with little effort.
5. Inspect the fiber face with an objective lens to gauge the quality of the fiber face.
6. If the cleave quality seems acceptable, about ~2cm of coating on the fiber is to be burned away beginning at the cleave point. This can be done with a simple Bic lighter. Burning away the coating is crucial as the coating melts at a much lower temperature than silica and during the beam focusing into the fiber, we do not want to burn any coating that may block the fiber face or introduce debris within the fiber.

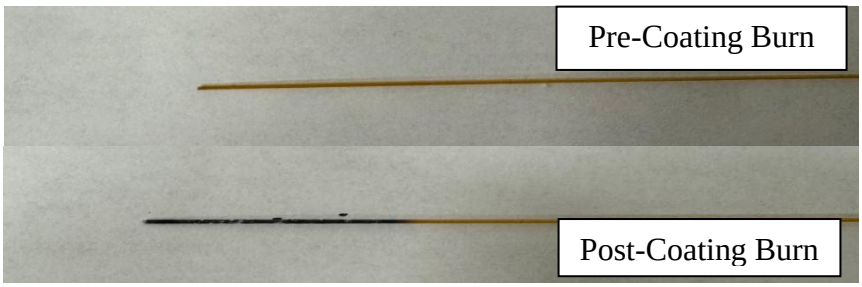

7. As the coating burns away, black residue will be left behind. Apply methanol or acetone to a clean tissue sheet and gently wipe away the remaining burnt coating.

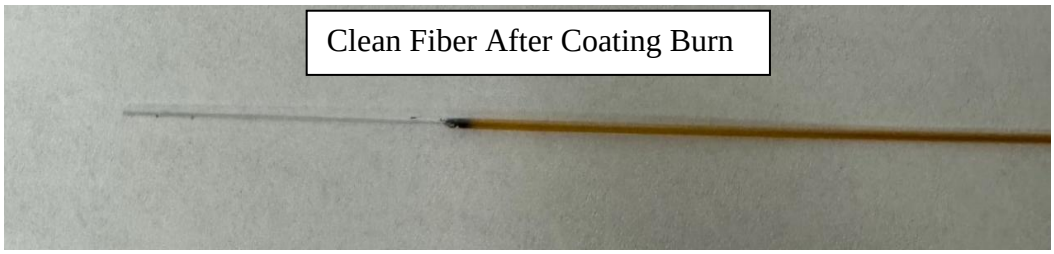

8. Inspect the fiber face once more and if acceptable, the other end of the fiber may be cleaved following the same procedure.

APPENDIX B

FIBER CLEAVING

Procedure:

1. Before gluing the fiber within the aluminum disk, mount down the micrometer stage and attach the 1” OD mirror mount. Clamp the aluminum disk within the mount.
2. Setup a post that supports a magnetic clamp which will hold the HCF we previously cleaved as shown, the height only needs to be approximately equal to the fiber pinhole of the aluminum disk.

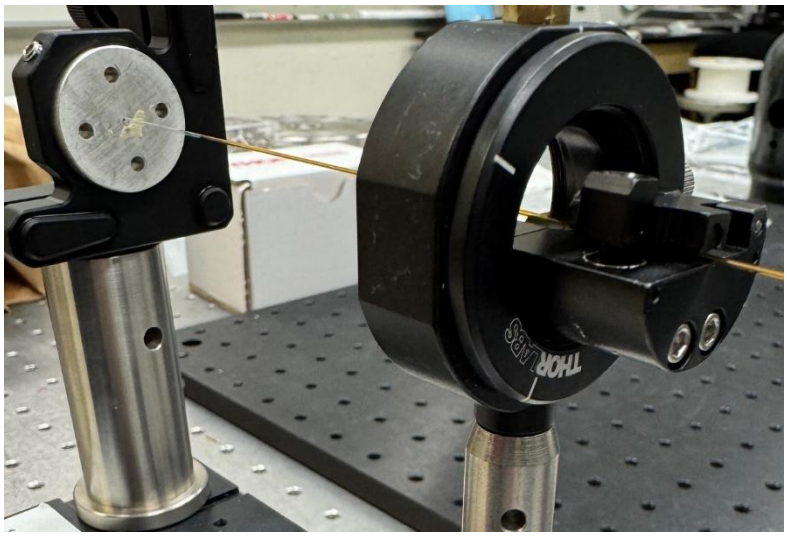

3. Lift up on the magnetic clamp such that you can feed the fiber through the aluminum disk pinhole until ~1cm is exposed beyond the aluminum disk. Exercise caution here as to not damage the fiber face while threading it through the pinhole. The fiber can bend during this process if it is not excessive.

4. Carefully adjust the height of the post supporting the magnetic clamp such that the fiber appears to enter and emerge the pinhole perpendicular to the aluminum disk. We want to minimize angle deviation in this step as it will complicate the beam coupling into the fiber.
5. When the fiber appears perpendicular to the aluminum disk, we can now prepare our "glue" which is a two-part epoxy resin. Torr Seal was the brand used for this thesis. The two-part resin should be mixed thoroughly for at least a minute. There is a ~15minute working window before the resin begins to harden.
6. Gently apply the epoxy mix to both ends of the pinhole. Be very careful not to accidentally apply any epoxy to the fiber face. Ensure that the application is even around the pinhole.

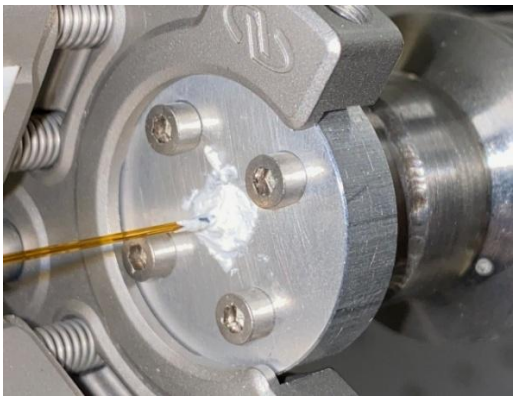

7. To glue in the other end, unclamp the magnetic mount and remove it from the setup. Replace it with a larger V-groove mount as shown below. Feed the fiber through the aluminum disk with caution as was done before.

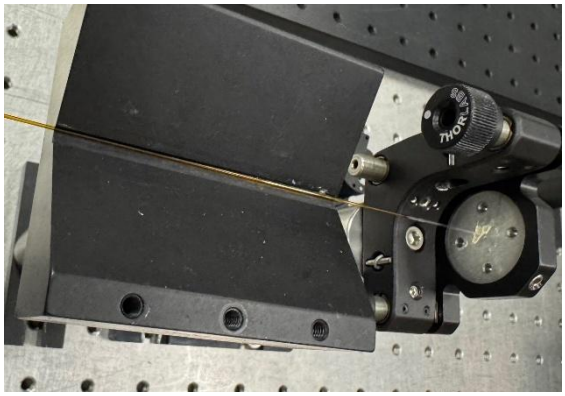

8. Adjust the height of the V-groove such that the fiber end emerges from the pinhole with no apparent bending and with ~1cm exiting the disk.
9. Glue this fiber end just as was performed earlier.
10. The V-groove can be lowered and removed from the setup once the resin has cured. The cure time requires 24 hours.

APPENDIX C

ACHIEVING SUFFICIENT TRANSMISSION

Much of the initial beam path work and positioning of the fiber is covered within Chapter 3.3.1 of this thesis. Here I will detail how to maximize transmission assuming the focused beam is striking somewhere on the fiber face. Make sure input pulse energy is below 50μJ while optimizing transmission!

Procedure:

1. Ensure that the fiber is stretched such that it appears straight without any radius of curvature. This can be done with the "z-axis" control knob of the micrometer stage. Do not over tension the fiber, apply just enough tension to eliminate any bending. Final tension optimization will be performed later.

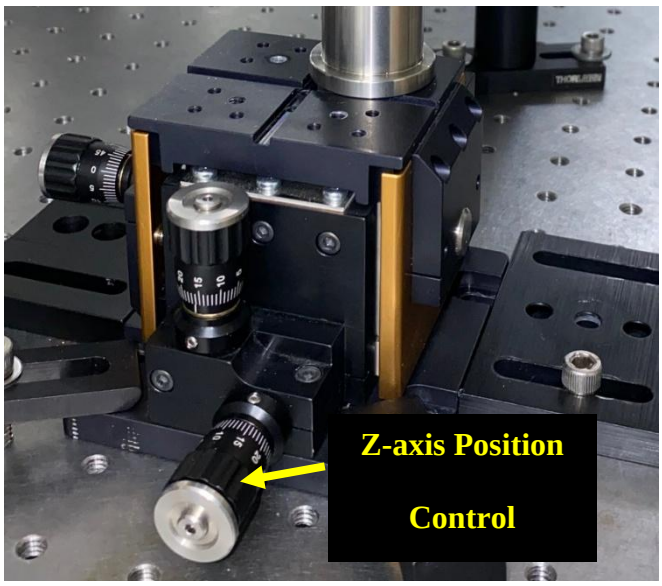

2. Measure the energy of your pulse just after exiting the focal lens before the entrance window of the HCF setup.
3. The beginning steps are to adjust only the micrometer stage positions in the vertical and horizontal plane on the entrance side of the setup. Measure the pulse energy exiting from the HCF setup and aim to maximize it. At this point transmission may still be very low but do not worry. Often the transmission spikes when we adjust the angular positioning of the fiber face in the next step.

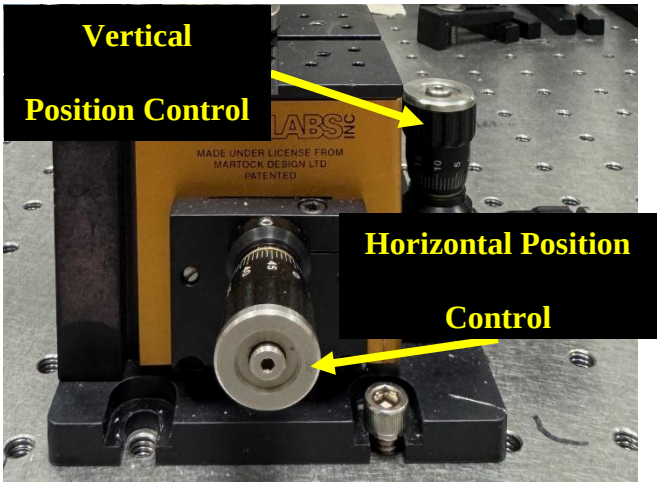

4. Before adjusting the mirror mount that controls the tip-tilt of the fiber we need to relieve some of the tension in the fiber via the “z-axis” knob. Depending on how the mirror mount is adjusted, tension is either added or reduced and we must be very careful not to introduce too much tension. This raises an issue that must be addressed. If we relieve/add tension beyond the optimal point, transmission efficiency will drop. This is a consequence we cannot avoid, so as we go optimizing transmission, we must stay cognizant of the stretched fiber. Very lightly tapping the fiber with your finger is a good gauge for how stressed the fiber is. Luckily for us, angular adjustments of the fiber tend

to spike transmission overshadowing loss from tension effects, giving a clear indication if you are adjusting in the right direction.

5. Working with just the entrance side of the fiber, adjust the fiber mirror mount while tracking the transmission efficiency. As you close in on the angular positioning of the fiber, adjust the horizontal and vertical positioning on the micrometer stage again as a new optimal position has likely occurred.

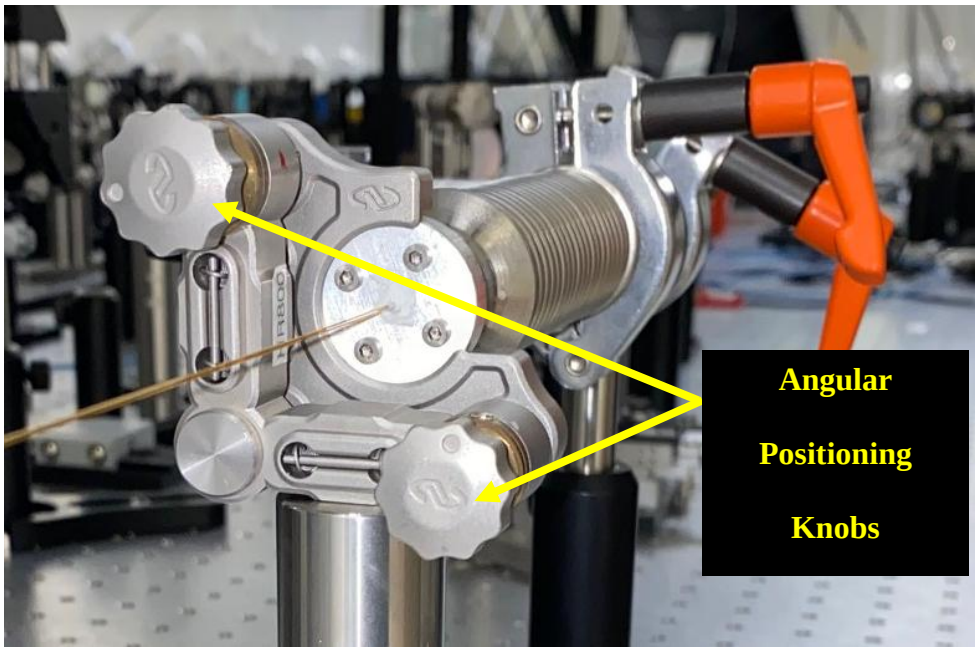

6. With the front end of the HCF optimized, the exit end can be adjusted. From my experience, only the tip/tilt mount has any noticeable effect on the transmission from this end. You may try adjusting the horizontal and vertical positioning as there is a chance it may improve the transmission efficiency.
7. When the micrometer stage and angular mount positioning are believed to be optimized, the last check is to adjust tension for maximum transmission. For reference, utilizing a 400nm input beam with a 70cm long 150µm ID and 30cm long 100µm fiber, I achieved

>50% and >35% respectively. At 267nm the transmission efficiency was >40% and >30% for the same fiber variants.